

A Study on Insulation Problems in Drive Fed Medium Voltage Induction Motors

by

Saeed Ul Haq

A thesis

presented to the University of Waterloo

in fulfillment of the thesis requirements for the degree of

Doctor of Philosophy

in

Electrical and Computer Engineering

Waterloo, Ontario, Canada, 2007

© Saeed Ul Haq 2007

I hereby declare that I am the sole author of this thesis.

I authorize the University of Waterloo to lend this thesis to other institutions or individuals for the purpose of scholarly research.

Saeed UI Haq

I further authorize the University of Waterloo to reproduce this thesis by photocopying or by other means, in total or in part, at the request of other institutions or individuals for the purpose of scholarly research.

Saeed UI Haq

Abstract

The PWM (pulse-width-modulated) type voltage source converters (VSC) allow a precise speed control of induction motors with maximum achievable energy efficiency. However, the rapid growth of this technology has created quite a concern, as the PWM waveform produces complex transients that stress the motor insulation, to much severe levels, compared to the normal sinusoidal voltage waveforms. As a result, the machine may fail prematurely due to increased dielectric heating; high turn-to-turn stress caused by non-linear potential distributions; increased partial discharge (PD) activities due to overshoots in pulse waveforms; and built-up space charge by high frequency signals. The present work therefore addresses the problems associated with enamelled wires and groundwall insulation in motor stator coil working under PWM-VSC.

In form-wound stator coils, the enamelled wires are meant to operate, mostly, at power frequency (60Hz) voltages. For PWM drive applications, it has been confirmed by using thermally stimulated depolarization current (TSDC) that the interfaces between the magnet wire insulation layers give rise to the accumulation of space charge that produces electric field perturbations inside the wire insulation. Numerical analysis further explored that this hazardous inter-turn electric field can be reduced up to ~48%, if the fewer number of insulation layers with similar over all thickness is used on the magnet wire. This reduction in field can be attributed to a lower accumulation of space charge during the aging duration and likely due to fewer number of trap levels.

To make the motor magnet wires less susceptible to high dV/dt , more resistant to PD, and to reduced space charge effects, a solution with new enamels, by adding inorganic nanofillers is suggested. In this regard, the wire specimens having fumed silica as nanofillers shows promising results compare to Al_2O_3 and TiO_2 . In wire coatings, a filler concentration up to 1% shows considerable improvement in the life expectancy under PMW waveforms. Also, reduction in the amount of accumulated charges is additionally observed, more than 60%, which is associated with the conduction current that becomes larger for nanostructure materials. Nanofilled materials release trapped charges more rapidly, and thus, the residual charge after long depolarization times is smaller than those with pure materials.

In groundwall, the insulation problems stemming from the use of PWM-VSC with medium voltage motors are mostly associated with the voltage stresses on the surface of the coils. PD erodes the mica layers, aggravating the problem and, perhaps, eventually destroying the whole stator insulation system. At present, there is no industrial standard available to evaluate the groundwall insulation life of motors fed from PWM-VSC. To observe variations in the life expectancy and to understand the degradation mechanisms, accelerated aging of groundwall insulation under steep-front unipolar pulses are carried out, considering the operating temperature range, pulse switching frequency, and voltages. Compared to 60 Hz ac, the maximum drop in the lifetime is observed to be ~58%, when the pulse voltage waveform with switching frequency up to 3 kHz is used under normal ambient temperature. However, with the use of efficient cooling, an improvement in the life expectancy of the groundwall insulation is predicted and the drop in the lifetime is observed to be ~31%.

Furthermore, as hot spots are observed in groundwall insulation with PWM-VSC aging the dominant mechanism is believed to be more thermal than electrical. However, the degradation caused by electrical aging, becomes much faster in the presence of hot spots, when the PWM-VSC is used. The visual examination of groundwall stator bars established that the presence of both thermal and electrical stresses produces much severe effects, leading to delamination, cracking, embitterment, or depolymerisation of the insulation system. In this regard, the obtained results further explored that the characterizing of groundwall insulation for better applications at higher temperatures and frequencies is therefore essential. In order to extend the lifetime of form-wound stator coils under PWM-VSC, this research strongly believes that the changes are required in the processing of the coils at the VPI and enamel coating stages.

Acknowledgements

I would like to thank my supervisors, Dr. Shesha Jayaram and Dr. Edward Cherney for their, assistance, support, and guidance throughout the duration of this work.

I am grateful to the members of my Ph.D. committee for their valuable suggestions and critical comments.

Thanks to both Dr. Gorur G. Raju from University of Windsor, and Dr. Greg Stone from IRIS Power, who provided me a kind support and did a number of discussions on academic and research, during my graduate studies.

Thanks to my friends of the high voltage group: Ali, Alex, Ayman, Chahat, Chitral, Emad, Fermin, Gowri, Isaias, Jason, Luiz, Mostafa, Rocket, Ron, Sarajit, Tilak, and Yushep, for all the nice moments that we shared in the HV lab.

Thanks are due to Ramtin Omranipour and Meredith Stranges from GE Peterborough for providing test samples and for their valuable comments during this work.

Also, I would like to thank all our Pakistani, Indian, and Canadian friends in Waterloo for their company during these years.

To my family, especially my wife Qamar Saeed, mother Pukhraj Begum, and my father-in-law Ashfaq Ahmed Paracha, I express my deepest gratitude for the support provided.

I gratefully acknowledge NSERC and the Ontario Ministry of Training, Colleges and Universities for financially supporting my graduate studies and the Water and Power Development Authority (WAPDA), for the X-Pakistan study leave.

To my loving wife Qamar
To my mother, sisters and brother

Table of Contents

Chapter 1 Introduction	1
1.1 Introduction	1
1.2 Stator Winding Insulation Systems	3
1.2.1 Strand and Turn Insulation	4
1.2.2 Groundwall Insulation System	5
1.2.3 Stress Grading System	7
1.3 PWM-VSCs Waveform Stresses	8
1.3.1 Stresses due to Nonlinear Voltage Distribution	10
1.3.2 Impact of Cable Length	12
1.3.3 Partial Discharge (PD) Erosion	13
1.3.4 Consequences of Space Charge	14
1.4 Literature Review	18
1.4.1 Space Charge Accumulation, Trapping and Charge Injection in Magnet Wire Coatings	18
1.4.2 Performance of Nanofilled Magnet Wires	20
1.4.3 Modelling	22
1.4.4 Evaluation of Groundwall Insulation	23
1.5 Aim of the Present Work, and Thesis Organization	25
Chapter 2 Materials, Experimental Setup and Modelling	27
2.1 Introduction	27
2.2 Materials	27
2.2.1 Magnet Wire Base Material	27
2.2.2 Nanofillers for Magnet Wire Overcoat	28
2.2.3 Turn-to-Turn Specimens for Insulation Test	31
2.2.4 Preparation of the Samples for the Groundwall Testing	34
2.3 Statistical Analysis	35
2.3.1 Weibull Analysis	37
2.4 Modelling of Systems with Inter-turn Stress	38
2.4.1 Finite Element Method (FEM)	39
2.5 Characterization of Stored Charge in Solid Dielectrics	40
2.5.1 Thermally Stimulated Depolarization Current (TSDC) Method	41
2.5.2 Stored Charge and Trapping Levels	43
2.6 Experimental Setup	43
2.6.1 PD Measurements	44
2.6.2 Temperature Measurements using an Infrared Camera	46
2.6.3 Measurement of the TSDC	48
2.6.4 Pulse Aging Test Circuit	50
2.6.5 SEM and Image Tool Software for Surface Roughness Measurements	55

Chapter 3 Results	57
3.1 Introduction	57
3.2 Enamelled Wires Aging Test	57
3.2.1 Effect of Steep-Front Pulse Voltage Waveforms	58
3.2.2 Effect of High Frequency AC Waveforms	63
3.3 Magnet Wires PD Erosion Tests	66
3.3.1 PWM-VSC Aging	66
3.3.2 High Frequency AC Aging	68
3.3.3 Residual Insulation Strength	70
3.4 Thermally Stimulated Depolarizing Currents (TSDC) in Magnet Wires	71
3.4.1 Long-Term Aging Effect (tP)	72
3.4.2 Influence of Polling Field (EP)	74
3.4.3 TSDC Measurements under PWM-VSC Waveforms	76
3.4.4 Effect of Multiple Layers on the TSDC Measurements	79
3.4.5 Stored Charge in Nanofilled Magnet Wires	80
3.5 Groundwall Insulation Tests	81
3.5.1 Thermographic Results of Groundwall Insulation	81
3.5.2 PD Measurement Results	84
3.5.3 Long-Term Aging Results	85
Chapter 4 Discussion	90
4.1 Introduction	90
4.2 Enamelled Wire Degradation Mechanisms	90
4.2.1 Influence of Voltage Waveforms	91
4.2.2 Consequence of Space Charges	92
4.2.3 Relationship between the Stored Charge and the Aging Time	93
4.2.4 Trap Activation Energy	95
4.3 Nanofiller Performance	98
4.3.1 Analysis of Weibull Distribution Parameters	101
4.3.2 Relationship between Relative Surface Roughness and Frequency	105
4.3.3 Effect of the Surface Roughness on the DC Breakdown Strength	107
4.4 Aging Mechanisms in Groundwall Insulation	107
4.4.1 Performance of the Groundwall Mica Tape	108
4.4.2 Visual Examination of the Failed Stator Bars	109
4.4.3 Mechanisms of the Failure in Groundwall Stator Bars	111
Chapter 5 Conclusions and Suggestions for Future Work	115
5.1 Summary	115
5.2 Conclusions	118
5.3 Suggestions for Future Work	120
References	122

Appendix A: Inter-Turn Model	137
A1. Numerical Analysis	138
A2. Influence of Pulse Rise Time	142
Appendix B: Space Charge Measurements using PEA	144
Appendix C: List of Publications	146
C1 Papers in Refereed Journals	146
C2 Papers in Refereed Conferences	147
C3 Non-refereed Presentations	148

List of Tables

Table 1.1: Voltage drop across the turns of the coil (% of the applied voltage) as a function of the cable length, L (m)	11
Table 2.1: Polyimide (ML® RC-5019), magnet wire base material properties	28
Table 2.2: Properties of selected rutile titanium oxide, TiO ₂	29
Table 2.3: Properties of selected fumed silica, SiO ₂	30
Table 2.4: Properties of selected alumina, Al ₂ O ₃	31
Table 2.5: Parameter related to magnet wire	33
Table 2.6: Test conditions for groundwall aging	52
Table 3.1: Parameters related to medium voltage conventional magnet wires S ₁ and S ₂ , subjected to different pulse switching frequencies	59
Table 3.2: Dimensional and electrical parameters, related to magnet wires having coating type polyimide, Pyre-ML®, before aging (Reference Data)	63
Table 3.3: Average, mean, and standard deviation of the relative surface roughness in magnet wire coatings subjected to PWM-VSC waveforms at 100 kV _p /mm.....	67
Table 3.4: Average, mean, and standard deviation of the relative surface roughness in magnet wire coatings subjected to high frequency ac waveform at 70 kV _p /mm	69
Table 3.5: Test conditions for TSDC measurements	72
Table 3.6: Comparison of PDIV (kV peak) levels for different test conditions	85
Table 4.1: Constants in Equation (4.2) obtained from the curve fitting procedure using the least square method, for relative surface roughness of specimens subjected to voltages of different ac frequencies at a constant electric stress.....	106
Table A1. Polyimide coated magnet wire (S ₁) electrical and physical constants, and parameters for numerical analysis	140

List of Figures

Figure 1.1: Cross-section of coils, identifying different insulation systems	4
Figure 1.2: Cross section of a multi-turn form-wound motor coil	5
Figure 1.3: Measured voltage waveforms with overvoltage situation at the terminal of a star connection motor for a two-level converter	9
Figure 1.4: Measured pulse voltage for each turn in a single form-wound 4.0 kV stator coil having rise time of ~100 ns.....	11
Figure 1.5: Origin of PD on stator winding insulation system.....	14
Figure 1.6: Energy band model in polymers containing electron and hole traps	16
Figure 2.1: Cross section of magnet wire showing coating layer.....	32
Figure 2.2: Turn-to-turn samples geometry.....	34
Figure 2.3: VPI stator bars with single layer of mica flakes tape (a) bars received from manufacturer, (b) divided into three test areas.....	34
Figure 2.4: A six-layer system for evaluation of groundwall insulation	35
Figure 2.5: Electrical Connection for PD measurement using XTrac™	44
Figure 2.6: An example of the oscilloscope trace of a PD signal, along with the output voltage waveform from the detector	45
Figure 2.7: Image recorded using CoroSMART Camera (optical detector) with corona discharge activity	46
Figure 2.8: Temperature measurement system.....	47
Figure 2.9: Measured temperature on the surface of the 4.0 kV _{L-L} form-wound stator coil energized at 2.5 kV peak ($f_s = 2$ kHz).....	47
Figure 2.10: Schematic of an experimental arrangement for the study of TSDC	48
Figure 2.11: Thermal protocol and steps for the measurement of TSDC.....	49
Figure 2.12: Schematic of TSDC in polymers	50
Figure 2.13: High voltage pulse modulator used for endurance test	51
Figure 2.14: Schematic representation of circuit employed for pulse endurance test	52
Figure 2.15: Stator bar specimens used for evaluation at high temperatures	53
Figure 2.16: FFT spectrum of the PWM drive (Modulation frequency: 3-4 kHz).....	54
Figure 2.17: High frequency test voltage source.....	54
Figure 2.18: Comparison of SEM images for surface roughness measurements	56
Figure 3.1: Defects found in magnet wire coatings.....	59
Figure 3.2: Weibull probability distribution plot of the dc breakdown voltages for wire S ₁ at different pulse switching frequencies	60

Figure 3.3: Residual life based on the dc breakdown voltage for conventional wires aged by unipolar steep-front pulses at different repetition rates (aging voltage $S_1 = 1100 V_p$; $S_2 = 750 V_p$ for ~ 100 h duration).....	61
Figure 3.4: Variation in the shape parameter β and standard deviation σ for magnet wire S_1 under different pulse repetition rates. The log-log sub-plot shows the relation between the relative standard deviation σ/β and pulse repetition rate.....	62
Figure 3.5: Residual life based on the dc breakdown voltage for laboratory developed wires, aged by unipolar steep-front pulses at different repetition rates (test voltages, $S_{1A} = 215 V_p$; $S_{1B} = 390 V_p$; $S_{1C} = 570 V_p$; $S_{1D} = 720 V_p$ for ~ 100 h duration).....	64
Figure 3.6: Residual life based on the dc breakdown voltage for conventional wires (S_1 and S_2) aged under high frequency ac waveforms at a constant electric stress of 30 kV/mm peak for ~ 100 h duration.....	65
Figure 3.7: Residual life based on the dc breakdown voltage for laboratory developed wires aged under high frequency ac waveforms at a constant electric stress of 30 kV/mm peak for ~ 100 h duration.....	65
Figure 3.8: PWM waveform from a PWM generator used for testing of magnet wire specimens (S_1 to S_6).....	66
Figure 3.9: Summary of the PD erosion test results for magnet wires (S_1 to S_6) aged under PWM-VSC waveform at a constant stress of 100 kV _p /mm ($f_s = 1.25$ kHz). Bar mark the 5 and 95 percentiles; the extremities of the hatched box are 25 and 75 percentiles and the centre line represents the average of the data.....	68
Figure 3.10: Summary of the PD erosion test results for magnet wires (S_1 to S_6) aged under high frequency ac waveform at a constant stress of 70 kV _p /mm ($f = 10$ kHz). Bar mark the 5 and 95 percentiles; the extremities of the hatched box are 25 and 75 percentiles and the centre line represents the average of the data.....	70
Figure 3.11: Variations in the dielectric strength of magnet wires (S_1 to S_6) by increasing the ac frequency	71
Figure 3.12: TSDC results for time dependence pulses aged at 1 kV peak (pulse repetition rate – 2 kHz)	73
Figure 3.13: Total charge vs. polling time for magnet wire S_1	74
Figure 3.14: Effect of the polling field on the TSDC spectra of wire specimens for $T_p = 120$ °C, $t_p = \sim 1$ hr: steep-front unipolar pulse (1) 1 kV _p , (2) 1.5 kV _p , (3) 2 kV _p , (4) 2.5 kV _p , (5) 3 kV _p , (6) 3.5 kV _p	75
Figure 3.15: Total charge versus polling field for magnet wire S_1	76
Figure 3.16: Effect of PWM-VSC waveforms on TSDC spectra of small bar specimens.....	78
Figure 3.17: Total charge versus PWM-VSC output voltage, for magnet wire S_1	78
Figure 3.18: TSDC results for small bar specimens having enamelled wires with different insulation layers.....	79
Figure 3.19: Total charge versus number of insulation layers.....	80
Figure 3.20: Comparison of stored charge released using TSDC measurements.....	81

Figure 3.21: The identification of hotspots using infrared thermographic camera under 60 Hz ac, 5.0 kV peak.....	82
Figure 3.22: The identification of hotspots using infrared thermographic camera under 3.5 kV peak pulse, at 3 kHz.....	82
Figure 3.23: Temperature rise in groundwall insulation of stator with an increase in switching frequencies	83
Figure 3.24: PD pulses from the stator bar groundwall insulation at room temperature before and after pulse aging subjected to 5 kV peak at 3 kHz.....	84
Figure 3.25: Log-log plot of the duration versus stress at different switching frequencies and at normal ambient temperature	87
Figure 3.26: Comparison of life curves under ambient and forced cooling environments	88
Figure 3.27: Log-log plot of the duration versus stress at different switching frequencies and at a test temperature of 155 °C.....	89
Figure 4.1: Relation of the relative charge and aging time under steep-front unipolar pulses evaluated at a constant stress	94
Figure 4.2: Relaxation time obtained from the TSDC studies as a function of 1000/T in magnet wire S ₁ specimens aged at different durations under constant stress	95
Figure 4.3: Relaxation time obtained from the TSDC studies as a function of 1000/T in magnet wire S ₁ specimens aged under different polling voltages for a constant duration.....	96
Figure 4.4: Relation between the polling voltages versus the activation energy	97
Figure 4.5: Effect of insulation layers on the activation energy	98
Figure 4.6: Comparison of schematic illustration of the erosion process on nanoparticles surface in magnet wire with a constant stress of 70 kV _p /mm.....	99
Figure 4.7: SEM images of commercially available magnet wire with PD resistant coating with alumina as the nanofiller (PWM aging); having average surface roughness of S ₂ ~327 nm and S ₃ ~313 nm	101
Figure 4.8: Shape parameter values obtained form the Weibull distribution for wire specimens aged at 10 kHz ac.....	102
Figure 4.9: Relation between relative standard deviation (σ/σ_{\min}) and Weibull shape parameter, β values obtained form the Weibull distribution for wire specimens aged at 10 kHz ac.....	103
Figure 4.10: Effect of SiO ₂ (fumed silica) nanofiller concentration on dc breakdown strength	104
Figure 4.11: Images of wires having different filler concentration in wt%	105
Figure 4.12: Relative surface roughness N _R , of magnet wire specimens exposed to voltages with different ac frequencies at constant stress of 70 kV _p /mm	106
Figure 4.13: SEM photographs of mica-tape before and after breakdown, subjected to steep-front unipolar voltage pulses; (a) mica virgin sample, (b) pulse aged specimen, (c) mica-tape after pulse breakdown, (d) magnified breakdown area of (c) in mica-tape.....	109

Figure 4.14:	Degradation of the edges and bent areas in three different stator bars (top view).....	110
Figure 4.15:	Damaged areas in the groundwall insulation after the steep-front pulse aging in the stator bar	111
Figure 4.16:	DC breakdown voltage versus temperature for VPI groundwall stator bar specimens having single layer of mica-tape	112
Figure 4.17:	Surface temperature profiles for the stator bar groundwall insulation tested under pulse aging of 5 kV peak at 3 kHz and normal ambient temperature.....	113
Figure A1:	Different insulation systems on a form-wound coil.	137
Figure A2:	Microscopic picture of a commercial magnet wire S ₁ (Mag: 900x).....	138
Figure A3:	Stator inter-turn model along with the selected area for space charge influenced field calculation; (1) and (2) represent magnet wires, and (3) shows polyimide based multilayer insulation system between consecutive wires	139
Figure A4:	Approximation of measured PWM drive pulse voltage waveform, considered for the transient FEM simulations	140
Figure A5:	Form-wound stator intern-turn electric field behaviour with time due to space charge accumulation for pulse voltages with different rise times	141
Figure A6:	Form-wound stator intern-turn electric field behaviour by reducing the number of layers and keeping the coating thickness constant on magnet wire, for pulse rise time 40 ns.....	142
Figure A7:	Effect of the pulse voltage rise time on the inter-turn stress distribution	143
Figure B1:	Charge profiles obtained at different polling time for magnet wire S ₂ (applied voltage: 1500 V)	144
Figure B2:	Polarisation and depolarisation (volt-off) charge profiles, for magnet wire S ₂ (applied voltage 1500 V)	145

Chapter 1 Introduction

1.1 Introduction

The ac induction motor is the dominant motor technology in use today, representing more than 90 percent of installed motor capacity. These motors are available in single-phase and poly-phase configurations, in sizes ranging from fractions of a Watt to tens of thousands of Watts in output. A combination of an adjustable speed drive (ASD) with induction motor results in a high efficiency system, which can cover a wide range of applications. Therefore, due to the advantage of choosing the right-sized, energy efficient motor and to integrate it into an optimized drive-power system, the application of these motors is rapidly increasing [1].

In the early nineties, ASDs have been the linchpin, for precise speed control, which is varied almost continuously at all levels of power. In particular, modern converters implement the pulse width modulation (PWM) technique to produce variable frequency ac voltage waveforms, which are used in drive control. These PWM-type inverter drives allow for a more precise control of motors, than older technologies, which use variable voltage inverters (VVI), and current source inverters (CSI). In addition, such installations increase energy efficiency as much as 50%, improve the power factor and process precision, and provide other performance benefits such as soft starting and over-speed capability [2].

In a motor, the stator winding consists of strand, turn, and groundwall insulation. Typically, they consist of a combination of organic and inorganic materials. The groundwall, or slot insulation, is composed of epoxy-mica flakes on a fibre glass mat with a glass backing that separates the winding from the stator core; whereas, the turn insulation in the stators has an organic coating of polyimide. In windings where the turn and strand insulation differ, the turn insulation is usually a resin rich mica-paper tape.

Typically, this tape consists of small bits of mica flakes that are bonded to a fibreglass tape and wrapped around the insulated copper strands in the turn [3,4].

In medium voltage motors (≥ 1000 and ≤ 13800 volts), the form-wound stator coil insulation system is much more complex than the random-wound one (< 1000 volts). In addition to the use of mica flakes tape, bonded with epoxy or polyester resin as the groundwall insulation, the insulation system of a coil includes a semi-conducting coating over the slot-section of the groundwall. Also, a special coating is applied at the ends of the slots to grade the electric stress in these regions. Presently, both groundwall and enamelled wire insulation are designed to operate, mostly, at power frequency voltages (60 Hz). Therefore, in PWM drive applications; which has fundamental component of 60 Hz, the fast switching produces complex transients that severely stress the motor insulation. As a result, a machine can fail prematurely due to the increased dielectric heating; high turn-to-turn stress, caused by the nonlinear potential distributions; increased partial discharge (PD) activities, due to overshoots in pulse waveforms; and built-up space charge by the high frequency signals.

As there are continual developments in power electronics, the industry is focusing on devising drives for medium voltage motors with switching devices which can both turn on and off with rapid transitions to reduce switching losses [5]. However, this is at the cost of additionally stressing the motor insulation. The premature failure of motor insulation appears to be associated with an accelerated degradation, caused by the following:

- An increased growth rate in the material's micro-cavities due to the local electro-mechanical energy storage and failure of stress grading due to high frequency components, as they are particularly designed for power frequency only [6].
- Dielectric heating that usually occurs because of high repetition rates and frequency components [6,7].
- Space charge injection/accumulation in the wire's enamel due to the high voltage wavefronts, (dV/dt) , and frequency components [8].
- PD activity due to overshoots in the voltage waveform [9,10].

Overall, the progress in insulation technology has been slow and the few improvements are implemented only after a long and extensive evaluation. The introduction of new materials with higher thermal and electrical properties is essential for long-term reliability to avoid the above recognized problems. So far, with the conventional ac, the designs are optimized, so as to minimize the insulation degradation. However, problems of premature failure of medium voltage rotating machines, when fed by inverters must be addressed immediately, as it can affect the motor manufacturers standing. Although, different topics, related to the use of such power supplies have been investigated, the time has come to explore the physical mechanisms that are involved in the aging of insulating materials.

Therefore, the main objective of this thesis is to provide a comprehensive understanding of the degradation processes of medium voltage form-wound stator coils, in particular, within mica-based groundwall and turn-to-turn insulation, when they are exposed to various types of voltage waveforms [11,12,13]. More in depth knowledge of degradation mechanisms in form-wound stator coils will provide a better understanding of the phenomena responsible for accelerated aging and a better direction in the design and manufacturing of new materials and insulation systems.

1.2 Stator Winding Insulation Systems

To understand the design of a form-wound stator coil, various insulation systems are briefly described. The stator winding insulation system contains several components and features, which combined ensure that the required electrical isolation exists. The basic stator insulation systems that will be discussed in the following three subsections are composed of:

- Strand (or sub conductor) insulation
- Turn insulation
- Groundwall insulation

- Stress grading system

Figure 1.1 shows the cross-section of coils identifying different insulations in both random-wound and form-wound stator. Normally, the stator has two coils per slot in both medium and high voltage applications.

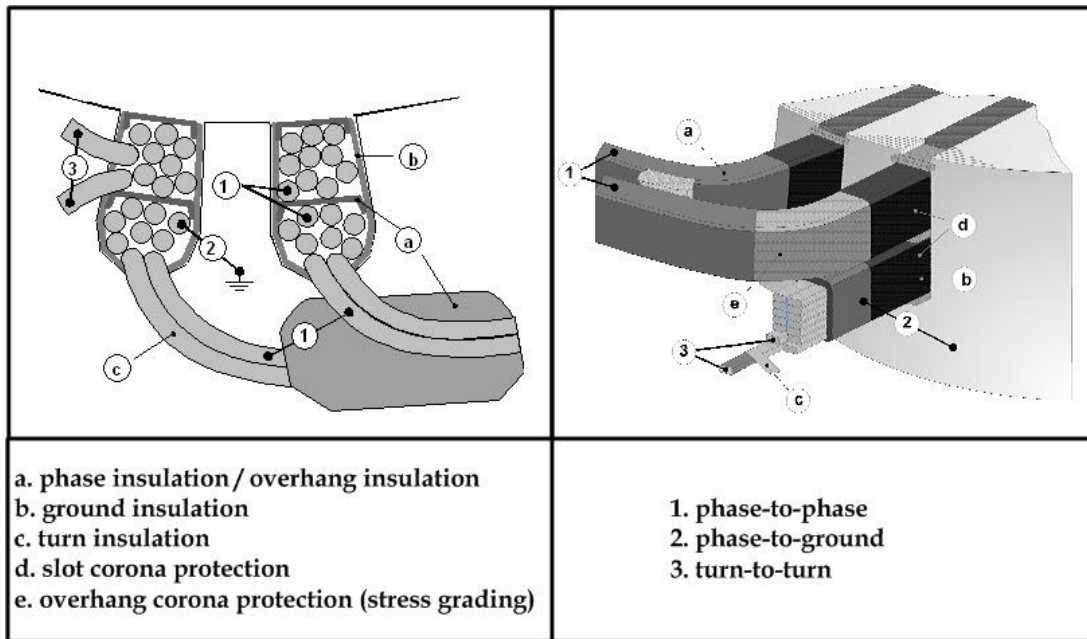


Figure 1.1: Cross-section of coils, identifying different insulation systems [14].

1.2.1 Strand and Turn Insulation

Typically, low-voltage motors are random-wound with round wire, insulated with polyamide-imide insulation or polyester with a polyamide-imide overcoat, having thermal class of 220 °C. Medium to high voltage motor are form-wound by rectangular shaped wire or strands. Such coils are divided into a number of turns that must be well insulated from each other. The cross-section of a typical form-wound stator coil showing strand insulation is depicted in Figure 1.2.

In multi-turn coils, the strand insulation can also be the turn insulation, a demand that, in the past, was met by separately wrapping resin rich mica tape. Often, this step can be

avoided by upgrading the strand insulation through machine tapping individual strands with a thin mica flake tape, supported with a polyethylene terephthalate (PET) or imide polymer film.

The magnet wire coatings in the form of enamel or polymer film may also contain additives such as alumina or special materials with a natural resistance to discharges, to protect it from PD [4]. Such corona-resistant enamels have been used since 1985 as turn insulation. The advantages are enhanced voltage endurance life, allowing reductions in the groundwall insulation thickness, and higher turn-to-turn surge withstand capability. However, the behavior of corona-resistant enamels is critical in today's variable speed drive applications [15]. In long-term, the continuous PD and overheating can cause shorts between the two strands, compromising the integrity of inter-turn and groundwall insulation systems.

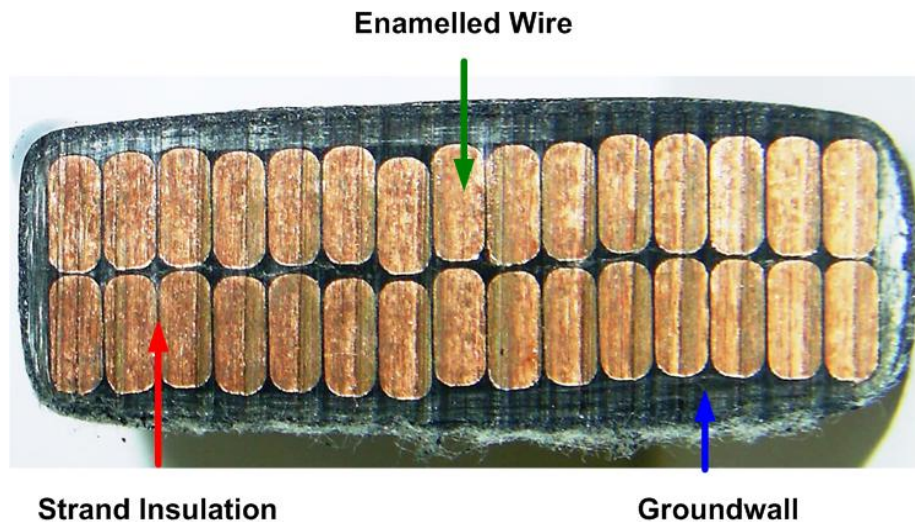


Figure 1.2: Cross section of a multi-turn form-wound motor coil.

1.2.2 Groundwall Insulation System

In the motor industry, the mica-based groundwall insulation system still predominates, where high voltage discharge effects and thermal stressing exist. The predominant mica species used in insulation systems are muscovite mica and phlogopite mica [16]. Mica, combined with different carriers, is considered the foundation of insulation systems.

These carriers are a mechanical support for the mica paper. Without them, the mica flakes cannot be applied to the conductors due to its own inherent low tensile strength. Currently, the commonly used carriers include films, fleece or mats, and glass fabrics [17].

The main purpose of the groundwall insulation system is to separate the copper conductors from the stator core. Usually, groundwall insulation failure triggers a ground fault relay. For a long service life, the groundwall must meet the rigors of the electrical, thermal, and mechanical stresses that it is subjected to. This class of insulation has additional stress relief coatings, which are important components in stator windings that operate at 4.16 kV or above [4]. These coatings are necessary to prevent PD from occurring on the surface of the stator bars or coils, and are described in the Section 1.2.3.

Common Groundwall Insulation Systems

Varnish Cambric (Class A 105 °C): In this class of insulation, the material is fully processed and no further impregnation or cure is needed when used for form-wound coil and bar insulation. It can be applied as half-lapped tapes or as a combination of tape and sheet. Slot pressing may be done to squeeze out the air between layers of the material and when heat is applied, the varnish softens and becomes tacky and on cooling, a weak bond develops between the layers of tape. This method, developed in Europe, was named the Haefley process. Due to the absence of mica, this insulation system was usually restricted to 2300 V and below [4,18].

Synthetic Resin Bonded Mica Tape (Class F 155 °C): This class of insulation system consists of small mica flakes that are deposited on a glass fibre backing tape. Once the tape has been wrapped around on the conductors, the synthetic resin is cured at an elevated temperature and pressure. This technique offers the possibility of manufacturing nearly void-free insulation that can withstand high dielectric stress. This insulation system has been in use since the sixties [15,18,19,20].

Silicone Rubber (Class H 180 °C): Silicone rubber is preferred in applications that need to withstand high temperatures. Although, there is no mica in this system, it can

withstand PD well. Silicone rubber is susceptible to mechanical damage and therefore restricts the voltage level to 6.0 kV. Silicone rubber can be used together with mica to increase the voltage level; however, the costs for such an insulating system are higher than for an epoxy system [18]. Later on, it was found by the motor manufacturers that silicone tended to creep with time and pressure. Therefore, the intended use in the slot section of machines was changed to end connections, where there is little or no compressive stress applied to the outside insulation [15].

In addition to the above groundwall insulation systems, shellac micafolium and asphalt-bonded mica tape (Class B 130 °C) were also used from the early 1900s to the 1970s. The use of these systems was discontinued due to heavy PD erosion and poor heat transfer.

1.2.3 Stress Grading System

In form-wound coils, it is not unusual to include semi-conducting tape and filler materials in the slot portion. Such tape provides a good electrical contact to the slot wall due to its low resistance. The filler materials protect the groundwall insulation from physical damage, and fill the gap between the coil surface and the slot. To avoid shorting the stator core laminations, a material with constant conductivity (10^{-2} to 10^{-5} S/m), which shows little or no field dependence, is typically used [21]. Silicon carbide (SiC) has been commonly used while zinc oxide varistor material (ZnO-VM) is under study as a replacement for SiC. This provides voltage stress grading system to limit the erosion from PD [18]. These materials exhibit electric field dependency, such that, high conductivity exists only where the electric stress is high, and a low conductivity, where the field is low [22].

Although semi-conducting tapes, slot fillers, black armour materials and stress grading coatings for stator coil insulation systems have performed well under normal power frequency, their exposure to PWM voltage source converters (VSC) led to an early failure of these coatings. It is reported that the high-frequency voltage pulses, associated with non-sinusoidal power supplies, cause a more rapid deterioration of the surface of

black armour or at the coil ends. This is a crucial consideration in the design of machines intended for inverter drives employing fast switching devices [23,24,25,26].

In this thesis, the focus is on turn-to-turn and mica-based main groundwall insulation system. Stress grading systems are not part of any investigation, as considerable work has already been reported in reference [25], to understand the impact of fast repetitive voltage pulses.

1.3 PWM-VSCs Waveform Stresses

As mentioned in Section 1.1, to control the speed of the ac motor and the power flow, a conversion of dc to ac voltage is necessary. For a broad power range, the two main concepts for conversion are the voltage and current source converters. These two categories are distinguished by the dc-link energy storage technique, such as, the current source converter (CSC) needs a dc-link inductor; whereas, the VSC requires a dc-link capacitor. In the early stages of high power conversion, CSCs are attractive due to the tight control of the converter current. However, this type of topology has lost its prestige in the drives market, and VSCs have become the most popular converters due to their simple topology, high efficiency, ease of control, and fast dynamic response. The PWM method is the dominant technique used in VSCs to control the voltage output [25].

The design of the VSCs is quickly changing so as to provide higher voltages and faster switching devices with steeper wavefronts. The option of increasing the voltage rating is preferred over increasing the current rating because of the practical limitations of the power components: motors, cables, and transformers [27]. The rapid developments in power electronics have facilitated this trend [28]. At present, it is possible to produce a VSC from 2.4 to 13.8 kV for motor drives [29].

To produce medium voltage drives for motor control, two types of power electronic devices with increased capabilities are used: the insulated gate bipolar transistor (IGBT), and the integrated gate commutated thyristor (IGCT) [27,28,30]. Both devices are used in PWM-VSCs. With advantages such as a high switching frequency, low cost, and more

mature technology, the IGBT is more commonly used in high power high voltage VSCs [30,31]. To meet the demand of converter manufacturers, IGBTs rated at 3.3 kV and 6.5 kV and with currents of approximately 1000 A are now available, and devices at 10 kV are being tested [27]. For PWM-VSCs, different schemes or topologies for connecting the switches can be found; however, at low voltages, the two-level converter is the most common, because it is simple and cost effective and more reliable than the multilevel topologies [27,32]. At this time, there is no predominant topology in medium voltage drives. Multilevel topologies (more than two-level) are preferred. The simplicity of three-level topology makes it one of the most common systems. In the present state-of-the-art, a two-level topology could represent the best option, especially with the higher ratings of the currently available switches; the associate insulation problems discourage the motor manufacturers to adopt it [23].

The typical PWM voltage waveform from an IGBT-based VSC is shown in Figure 1.3. These pulses exhibit rise times of hundreds of nanoseconds. Even though, two or more IGBTs are usually connected in series (stacks), despite they can present a high dV/dt , typically 15 kV/ μ s in machines and much higher in power system applications [28].

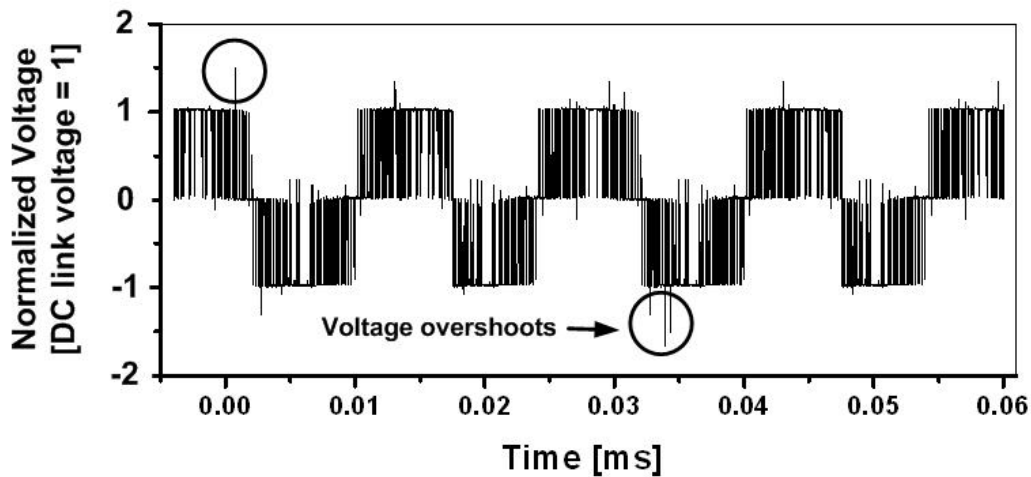


Figure 1.3: Measured voltage waveforms with overvoltage situation at the terminal of a star connection motor for a two-level converter.

A key point to make is that motors which were originally designed and manufactured to operate on sinewave 60 Hz power, are subjected to a significantly reduced dielectric life, when PWM voltage is applied: that is, a motor operating on sinewave power has a longer winding life expectancy than an identical motor operating on a PWM supply, if all the other stresses are constant.

1.3.1 Stresses due to Nonlinear Voltage Distribution

The increased use of PWM-VSCs has increased the stress on the winding insulation due to non-sinusoidal nature of the voltage waveform. Besides the amplitude, the steepness of the applied voltage is much higher than that of sinusoidal voltage. Consequently, the voltage distribution within the windings and coils is highly nonlinear and may cause voltage stresses between two consecutive turns [33].

According to Oyegoke [34] and Suresh *et al.* [35], the steep-front surges that strike a stator winding results in a large voltage across the inter-turn insulation in the motor coil, connected to the high voltage terminal. The distribution of the voltage across the high voltage motor coils is not uniform; that is, the high frequency content (in the megahertz range) of the surge voltage results in the capacitive division of the surge across the turn insulation, rather than controlled by the inductance. The shorter the rise time of the surge, the higher the frequency content and the voltage will be greater across the first few turns of the winding. The results of turn-to-turn voltage measurements for various coil ratings are summarized in Table 1.1 [34].

Figure 1.4 shows an example of nonlinear voltage distribution in 4.0 kV form-wound stator coil for a short rise time pulse (~100 ns). The voltage source is connected to the input end of the stator coil via cable. Detailed measurement of the voltage over each individual turn of coil is then performed. Each turn conductor of this eight-turn coil is exposed at appropriate positions to allow the measurement. The voltages are measured with respect to the stator core keeping it grounded throughout the measurements. The difference between the maximum voltages across individual turns represents the inter-turn stress. In such cases, if a motor winding is subjected to steep-front surges, the

breakdown strength of the turn insulation may be exceeded, causing a turn insulation breakdown, and eventually the groundwall insulation is affected [36].

Table 1.1: Voltage drop across the turns of the coil (% of the applied voltage) as a function of the cable length, L (m).

Coil Rating	# of Turns	Pulse Rise Time (ns)	Cable Length (m)	Voltage (% of the Applied Voltage)	
				Min	Max
4.0 kV ^a	8	100	1.5	5.5	16.8
			6.5	13.5	20.1
6.3 kV ^b	11	200	2.3	12.0	18.9
			4.0	14.2	19.2
			17.0	14.9	22.2
13.8 kV ^c	4	100	1.5	2.4	10.9
			6.5	2.1	14.3

^{a,b}Data obtained from reference [34]. Both coils are non-turn tape and coil in (a) has no stress grading system.

^cData obtained from laboratory measurements. Test coil has resin rich mica turn tape and 3.5" stress grading system.

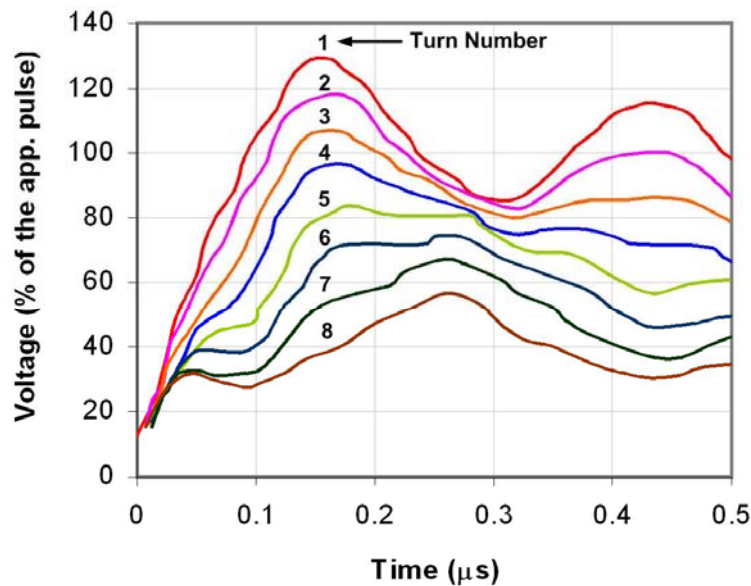


Figure 1.4: Measured pulse voltage for each turn in a single form-wound 4.0 kV stator coil having rise time of ~100 ns [34].

1.3.2 Impact of Cable Length

In many industrial applications, the inverter and the motor are at separate locations, requiring long motor leads. Although, the high switching speeds and zero switching loss schemes drastically improve the performance of the PWM drives, the high rate of the voltage rise (dV/dt) has an adverse effect on the motor insulation and bearings, and deteriorates the waveform quality where long cables are employed [37].

According to Bonnett [38], Wu *et al.* [39] and Lebey *et al.* [13], long cable lengths contribute to a damped high frequency ringing at the motor terminals, resulting in over voltages, further stressing the motor insulation. This ringing is due to the distributed nature of the cable leakage inductance and coupling capacitance (L-C). In addition, the voltage reflection is a function of the inverter output pulse rise time and the length of the motor cables, which behave as transmission lines for the inverter output pulses. It has been found that the pulses travel at approximately half the speed of light [40]. Moreover, if the pulse takes longer than half the rise time to travel from the inverter to the motor, a full reflection occurs at the motors, and the pulse amplitude is approximately double [12]. It is important that the insulation of the induction motor should be designed so that the insulation can withstand generated voltage stresses in the system. The stator winding overvoltages are based on the theory of voltage reflections. The motor cable behaves as a transmission line for the PWM pulses, and the voltage amplitude depends on the surge impedance of the motor [40].

In the mid 1990s, manufacturers introduced a combined motor inverter topology in which the inverter is integrally mounted within the motor enclosure, typically in the terminal box, or sometimes, as an extension to the motor casing. A very short cable length between the inverter output connections and the motor windings limits the reflection. As a result, the peak voltage problems do not exist. Due to the additional benefits of the simplified installation, reduced stress problems and lower costs, the topology is well suited for lower power applications, and is now rapidly gaining market acceptance [12]. However, problems still persist in large motor-drive systems due to space and cost issue during installations.

1.3.3 Partial Discharge (PD) Erosion

PD is a localized intermittent discharge, resulting from transient gaseous ionization in or on an insulation system, where the voltage stress levels exceed a critical value. Figure 1.5 illustrates some critical spots in the stator coil, which can cause PD activity.

Binder has provided some guidance for the acceptability of the discharge levels in machine insulation [41]. According to the author, machine insulation usually consists of mica, bonded with resin that has high discharge resistant. As a result, a discharge magnitude as high as 1000 pC is acceptable in the stator bars. However, if the discharge magnitude is within the range of 10-100 nC, the deteriorated bar should be located and replaced as soon as possible, since it can cause severe damage to the entire stator insulation system [41,42].

According to Shugg [43] and Stone *et al.* [36], the major factors that affect the PD or corona are voltage, frequency, temperature, voltage pulsation, humidity, geometry, dielectric thickness, and pulse rise time. The degradation of stator insulation that is exposed to a continuous voltage stress above the partial discharge inception level (PDIV) is a physical erosion of the insulation due to the PD attack. The aging process results from an erosion of the insulation material, reducing its thickness at the discharge sites, until its breakdown voltage capability is mitigated below the level of the applied voltage peak. However, if the voltage stress is below the PDIV, no premature degradation occurs [44]. Relatively little literature exists on insulation aging and PD development under fast repetitive voltage surges.

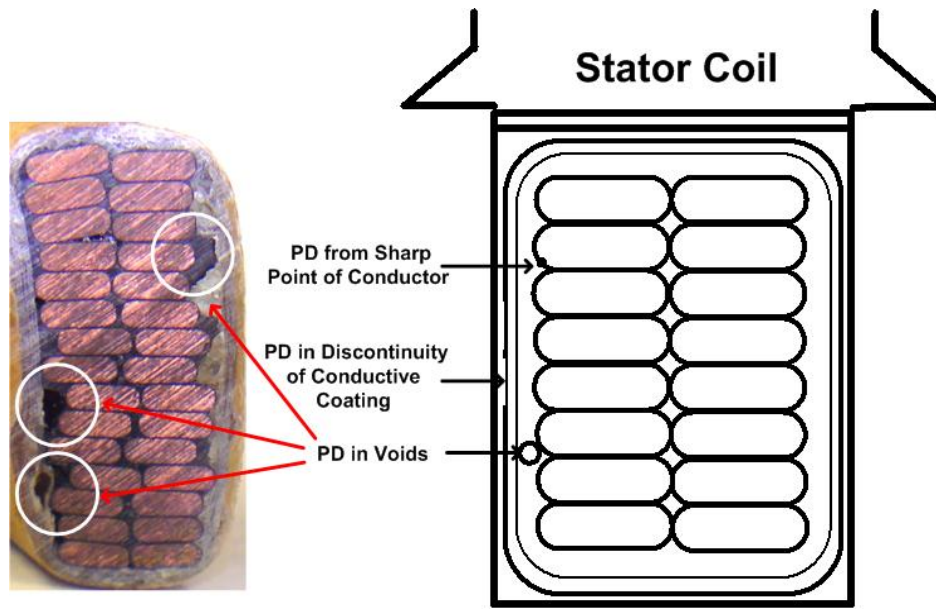


Figure 1.5: Origin of PD on stator winding insulation system.

1.3.4 Consequences of Space Charge

In PWM drive applications; the deterioration of magnet wire coatings can occur due to two detectable phenomena; namely, PD and charge trapping and injection. Furthermore, several investigators consider that the trapped charge carrier; establishing an electric space charge field, play an important part in the aging process [6,13].

The types of charge carriers in polymers and their role in conduction and breakdown have been presented by Idea [45] and Wintle [46]. There are four basic types of charge carriers possible in polymers: electrons, holes, positive ions, and negative ions. The principle charge carriers, which are important with reference to degradation, are believed to be electrons and holes. Polymers in terms of multi-layer arrangement provided considerable evidence for the existence of both these carriers from a large number of thermally stimulated current (TSC), pulsed electro-acoustic (PEA) method and photoconduction experiments [45,47]. However, the relative importance of electrons and holes is not so well established [48].

Carrier Injection

In polymers, the mobility of charge carriers has a significant effect on the conduction, tree initiation process, and degradation. At high values of electric fields (>1 MV/cm), where the electrons have sufficient energy to exist in the conduction band along polymers chains, much higher mobilities can occur. Before conduction can occur, there must be a source of charge carriers available. Some of these carriers could be liberated in the polymer bulk by radiation or extremely high electric fields, which are common in PWM-VSCs that are always acting on the trapped carriers. In practical situations, the most likely source of electrons and holes is injection from electrodes [48].

The three basic electrical mechanisms for injecting charge are Schottky-type emission, Fowler-Nordheim-type emission, and contact charging. The mechanism of contact charging will inject electrons or holes even when there is no external electric field [49,50]. Contact charging occurs because of the relative difference in the Fermi levels for the metal and polymer coating, and the existence of electron and hole traps between the valence band and the conduction band. Since the Fermi levels must be equal when the metal and polymer are brought in contact, charge is transferred to the polymer. This charge resides in relative deep traps, very close to the electrode. At moderate to high fields, electric field assisted thermionic emission, or Schottky emission, is one process. As, at higher stresses, adequate force is available from the field for the electron to be injected from the electrode; therefore, the injected current density (J) is given by the expression [49]:

$$J = AT^2 \exp\left[\frac{\alpha E^{\frac{1}{2}} - \Phi}{kT}\right] \quad (1.1)$$

where E , is electric stress, T , is temperature, Φ is metal work function and A , α , k are constants. According to Fowler-Nordheim, at higher fields, a greater number of electrons will gain sufficient energy to tunnel the barrier and J becomes [49]:

$$J = AE^2 \exp\left[\frac{-B\Phi^{\frac{3}{2}}}{E}\right] \quad (1.2)$$

The constants A and B in Equations (1.1) and (1.2) are conduction parameters, extracted from the experimental investigations [51].

Charge Trapping and Build-up of Space Charge

The trapping of electrons and holes plays a critical role in the build-up of space charges, conduction, and can probably cause slow degradation of magnet wire. Traps, by definition, are entities at a fixed location in the polymer, which attract either electrons or holes. In terms of energy, the traps have energy levels in the energy gap between the valence band and the conduction band. Hole traps are few tenths of an eV above the top of the valence band (shallow hole traps) or up to several eV above top of the valence band (deep hole traps). Similarly, shallow electron traps are just below the bottom of the conduction band; whereas, deep electron traps are several eV below the bottom of the conduction band. For clear description, a band model of a polymer containing electron and hole traps is depicted in Figure 1.6.

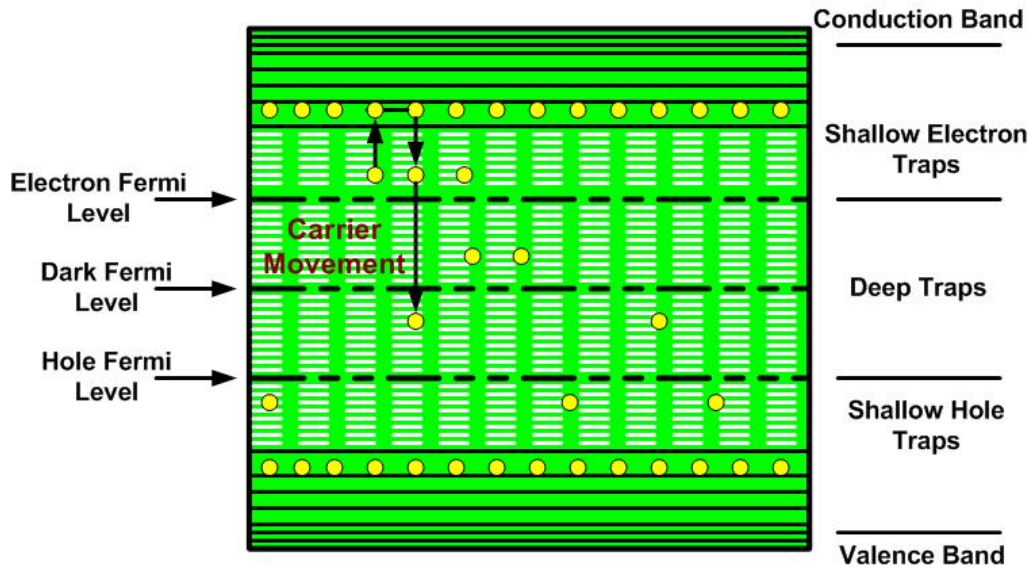


Figure 1.6: Energy band model in polymers containing electron and hole traps [52].

There are different causes of traps in practical polymers. The most probable types occur at the interfaces between crystalline and amorphous regions of the polymer, defects or dislocations in the polymer chain or side-chains, sharp bends or kinks in the polymer

chain, and at residual cross-linking agents. In such case, the TSC and thermally stimulated luminescence (TSL) studies are the most popular means of determining the trap energy levels.

Influence of PWM-VSCs Wavefront (dV/dt) on Space Charge

In PWM drive, the steepness of the wavefront (dV/dt) provides frequency components in the range of MHz. Thus, a possible relationship between the fronts and the dielectric response of the material exists. The presence of high frequency components, due to fast rise time voltage pulse produces maximum losses in the polymeric insulating materials, which are used in the motor stator coil.

The presence of such a component leads to a delay (out-of-step) polarization of some of the dipoles, and some of the charges might not disappear with voltage reversal. A sudden reversal of the voltage blocks the free charges of a particular sign, replacing them with free charges of the opposite sign. In fact, three types of charges are present on the surface of the insulation; that is, free charges, bound charges, resulting from a natural polarization; and blocked charges, which appear when the reversal of the voltage is too fast for certain types of dipoles. Once created, and independent of concentration, these charges, due to electrostatic forces, tend to move either perpendicularly or tangentially with respect to the surface. In the first case, the perpendicular movement creates a certain space charge in the bulk; whereas, in the second case, it corresponds to the charge flow on the surface. In the former, the electric field distortion ($\nabla \cdot E \neq 0$), is biased to the injection of new charges and this cumulative process may cause the breakdown of the material [11,13]. In the later case, distribution of charges over the surface can lead to a high surface charge concentration at particular points, e.g., at the slot ends. During the unavoidable phenomenon of recombination, a local breakdown of the surface can occur, damaging the insulation system [53]. Several factors, including temperature, relative humidity, vibration, the nature of the insulation, and its geometry can mitigate or amplify this phenomenon.

1.4 Literature Review

This section offers a review of the previous research on various aspects of both groundwall and turn-to-turn insulation. The previous work has been classified into principal categories: namely; the evaluation of the groundwall insulation in inverter-fed stator coils, the effect of a high wavefront (dV/dt) and frequency components on magnet wire coatings in terms of the space charge accumulation, trapping, and charge injection, the performance of discharge resistant nanofilled magnet wires, designed for inverter-duty applications, and the modelling of the inter-turn field distribution under steep-front voltage pulses.

1.4.1 Space Charge Accumulation, Trapping and Charge Injection in Magnet Wire Coatings

The impact of space charge accumulation on aging processes of polymeric insulating materials, subjected to PWM-VSC stresses has been widely neglected. The main reason is that, in addition to the space charge detection problem, the cause of the breakdown is mainly attributed to manufacturing features such as the presence of contaminants, cavities, protrusions and, in general, the defects that are able to trigger localized degradation processes such as PD and electrical treeing [54]. Consequently, for many years, failure was associated with “macroscopic” causes, rather than to microstructure.

Recently, the contribution of space charge to the insulation damage in stator windings is considered more carefully [55]. The presence of space charges, in the insulation bulk and/or at the insulation-electrode interfaces, can significantly affect the electric field distribution, and, in turn, the field concentration, inducing accelerated damage that triggers early insulation breakdown [13].

To understand the failure of low-voltage winding insulation, Yin [56] has performed an extensive investigation by using a square wave with a varying voltage level, frequency, duty cycle, and rise time. They have concluded that the failure of magnet wires under repetitive pulses, as seen in inverted fed motors, is not the result of a single

factor but of the combined effects of PD, dielectric heating, and space charge formation. The voltage overshoots that are produced by PWM drives can be above the discharge inception voltage (DIV). PD may therefore be present in inverter-fed motors. In addition to PD, pulses with fast rise time and high frequencies enable the insulation to generate local dielectric heating, which increases the local temperature. The degradation rate of the insulation, is therefore, increased. Furthermore, the fast rise and fall of pulses make it possible for space charge to accumulate in the winding insulation and on its surface. However, the investigation focuses on problems in random-wound insulation only [56].

Bellomo *et al.* [13] and Lebey *et al.* [57] have also reported on low-voltage stator insulation with particular respect to intrinsic aging under the working conditions of a voltage V , dV/dt , and frequency, where an interaction between the voltage characteristics and the material properties exist, that is, for V lower than the DIV. In conclusion, the existence of a new type of phenomena, the building and trapping of charges associated with these new stresses that is responsible for the slow degradation of turn insulation has been proposed. However, the authors have suggested that it is now necessary to quantify, in more accurate manner, the consequences on the lifetime of real systems.

In response to the new phenomena [13,57], Hudon *et al.* [8] have conducted tests which confirm that PD might not be the only mechanism responsible for turn insulation failure. Other mechanisms can contribute to the degradation of insulation, when it is subjected to PWM pulses, even at voltages below the DIV. Since these phenomena are related to the interaction between the applied voltage characteristics (e.g., frequency, dV/dt , and duty cycle) and the materials, such aging is intrinsic. These inherent degradation mechanisms can be related to charge injection and charge movement within the insulation. However, one conclusion is that a further understanding of the degradation mechanisms involved is still required [8].

Degradation mechanisms occurring in low-voltage magnetic wires fed by PWM waveforms were recently investigated by Fabiani *et al.* [6] through PD and space charge measurements. Their experimental results of space charge measurements showed a relation between space charge features (e.g. trap depth and trap-controlled mobility) and PD quantities (e.g. PDIV, PD amplitude and repetition rate). It has been shown that

inorganic-filled corona resistance materials do not exhibit always life improvements. However, insulation systems with increased surface conductivity or smaller trap depth (increased mobility) can present smaller partial discharges and thus, a longer life.

From the previous discussion, it is clear that space charge accumulation and trapping influence the performance of stator winding insulation. However, most of the studies have targeted low voltage random-wound motors and such phenomena are not well understood for high voltage insulation systems with ASDs.

1.4.2 Performance of Nanofilled Magnet Wires

In insulation, the use of nanofillers is very attractive for upgrading and diversifying the properties of polymers. Researchers, scientists, and practitioners across almost the entire spectrum of disciplines are exploring and developing science and engineering at the nano-level. Among these disciplines, the progress in the field of polymer sciences has demonstrated that the addition of nanofillers represents a very attractive route to upgrade and diversify material properties. There is a broad range of nanofiller types, which has led to nanopowders with different morphologies (size and shape, cluster composition, and dispersion) that are currently being used in PD resistant magnet wire coatings [58,59,60]. When the size of fillers is reduced to nanometer scale, it has been observed that usually, less than 10 wt% is enough to significantly change the material properties [60].

Hudon *et al.* [61] have reported that the nanofillers in magnet wire enamel are essential for a variety of reasons, including discharge resistance, matching the coefficient of the thermal expansion, thermal conductivity enhancement, mechanical reinforcement, and abrasion resistance. Based on the experimental and field results, manufacturers of magnet wires with fillers that have a uniform coating has become popular due to the growing use of ASDs. In ASDs, the repetition rate of the IGBT pulses increases substantially, and can be as high as 20 kHz with a rate of rise of several kV/ μ s. Because of the inductive nature of the winding, large reflections can occur at the motor end, and a significant portion of this voltage can develop across the adjacent turns. If the DIV is exceeded, this will lead to discharge activity. Therefore, in the presence of PD, fillers in

the material then form a line of defense to limit the erosion process and prevent further degradation of the insulating material [61,62].

To prevent PD erosion, enamelled wires with a multi-layered insulation system containing dispersed metal oxides have been marketed. Such wires have a three-layer structure, in which a PD resistant coating film is placed in between the normal coatings to compensate for the electrical and thermal properties. This structure is also helpful in the improvement of the mechanical properties. However, according to Kikuchi *et al.* [63], even though the wires life is improved, they are vulnerable to the electrical degradation due to the weakening of the materials, caused by mechanical stresses such as elongation, bending, and stretching. Such defects are potential areas for electrical degradation due to PD activity. Recently, alumina (Al_2O_3) nanoparticles have been successfully applied to film-coated magnet wires. The outcome has resulted in excellent electrical, thermal, mechanical, and physical properties of wires available for medium voltage applications. However, experimental investigation has demonstrated some large scatter in the breakdown data, suggesting that the mechanism needs to be examined [64].

The use of nano-meter-level particle size of silica (SiO_2), if dispersed uniformly, has exhibited a high level of resistance to PD; however, the SiO_2 concentration has a strong correlation with the wire flexibility, compared with that of other types of fillers [63,64]. As a consequence, the control of material properties, such as uniformity in the organic coatings and concentration (wt%) of nanoparticles, are major issues in wire nanotechnology. Increasing the loading (wt%) of nanofillers can further increase the PD resistance, but weakens the mechanical strength, influencing the electrical degradation. In this regard, Kikuchi *et al.* [63] have developed, a state-of-the-art inverter surge resistance enamelled wire, which is based on silica-polyesterimide nanocomposite material. This wire is specifically designed for low voltage applications, and proves to be satisfactory for PD resistance, flexibility, and mechanical strength.

In addition, a reduction of the amount of accumulated charges common to materials with nanofillers has been reported [65]. The variation in the space charge is associated with the conduction current that increases for nanostructural materials. These materials release trapped charges more rapidly, and thus, the residual charge after long

depolarization periods is smaller than that of pure materials [65]. Also, Nielson has examined the effects of nanofillers on space charge accumulation, but the insulation integrity of the nanocomposites is still not understood [66,67].

Brütsch and Weyl [68] have reported some results for the filled enamelled wires that are available in the market. The authors have suggested the use of filled enamelled wire with the problem that it may have little effect or no effect on the PDIV, but does reduce the rate of erosion under corona conditions. Furthermore, filled enamelled wires have a limited mechanical strength due to the brittleness of the coating.

Overall, the literature review indicates that under most operating conditions that are relevant to inverter-fed motors, PD resistant insulation lasts longer. This is valid when the voltage surges are large enough or above the DIV. However, around the DIV, the materials behave differently and the use of PD resistant insulation can even reduce a motor's life [62]. This assumption does not apply in all operating conditions, or for all types of PD resistant and standard insulation. It is possible that testing the insulation at higher voltages is not adequate to evaluate the insulation intended for PWM operation. A more comprehensive set of quality control tests still needs to be conducted, along with the development of new techniques, to adequately compare different nanofilled insulating materials [62].

1.4.3 Modelling

It has been accepted that space charge is one of the parameters that influences the degradation of motor insulation significantly under pulse energization. Although PWM waveforms are bipolar due to the fast polarity reversal of the potentials, space charge accumulation is possible, and experimentally, its presence has been observed. However, there are no analytical procedures available to calculate the space charge influenced field that can cause localized discharges.

The dynamics of the electric field distribution, influenced by the charge accumulation between two adjacent enamelled wires and in the complex geometry of the coatings can be determined by two methods: the equivalent circuit method and the finite element

method (FEM) [69,70]. New methods such as the boundary element method [71] or improvements to the existing models [72] have been suggested. The validation of such methods has been difficult, but a good approximation of the influence of the various parameters can be obtained with the proper use of these models. However, most of these comparisons between the simulations and experimental measurements have been carried out at low frequencies (50 or 60 Hz). There is an interest in verifying the reliability of the models that are used to study the effect of fast pulses. The difficulties with the measurements under fast pulses make this task difficult if not impossible, as there are no measuring techniques to determine the voltage or electric field distribution under voltage pulses.

As a result, it is important to compute the space charge injected electric fields in the motor insulation interfaces under pulse applications by using FEM. Since, the applied voltage is a steep-front short voltage pulse, a transient finite element analysis seems to be the best option for the computational studies. The effects of rise time and the accumulated charge with different concentrations on electric fields must be analyzed in simple geometries by using 2D software.

1.4.4 Evaluation of Groundwall Insulation

Several problems, relevant to reliable stator insulation system need to be considered and resolved, when medium voltage induction motors are fed from PWM-VSC. Due to some recent premature failures of motors fitted with adjustable speed drives (ASD), standards organizations such as the National Electrical Manufacturer's Association (NEMA) and International Electrotechnical Commission (IEC) are developing technical specifications to ensure that motors can withstand the increased stresses during their service life. In this regard, some of the initial standards are NEMA MG 1 Parts 30 and 31 [73], in which the inverter-duty motors undergo voltage impulses. However, it has been recognized that the short impulse test might not always ensure a satisfactory life. Similarly, the IEC TS 60034-25 [74], which provides a detailed discussion on motor insulation stresses and

methods for determining short-term withstand test limits, does not include the high-cycle fatigue conditions that motors undergo during their service life [75,76,77].

To complement the available test procedures, IEC TS 60034-18-42, which is under development, will propose a new test procedure for the qualification of groundwall insulation [78]. However, the inverter drive designers are employing higher voltages and faster switching devices with steeper wave fronts. There appears to be a lack of coordination between the motor manufacturers and the drive designers, which needs to be realized. Therefore, further experimental work is recommended for the establishment of a qualification scheme suitable for a variety of different inverter system designs [14,78].

Up to certain extent, the insulation performance of form-wound stator coils, rated at 4.16 kV for inverter-duty application, has also been investigated by Ramme *et al.* [44]. The parameters were the influence of voltage level, rise time, switching frequency, and temperature on the generation of PD for two different coil insulation systems. In their work, the authors did not study the insulation “life/aging” integrity test for longer duration. Accordingly, they have concluded that all the investigated factors influence PD inception, except the switching frequency. It has little effect on PD voltage inception levels but higher switching frequencies do generate a larger amount of external PD such that severe degradation occurs under inverter-fed conditions.

The literature review confirms that fewer investigations have been devoted to understand the fundamental problems associated with the dielectric breakdown of groundwall insulation under high frequency transients [79]. Although some work has been conducted in this area [26,44], experimental results are still lacking. So far, most of the investigations have been carried out in the random-wound motor stators (Type I insulation) [14]; whereas, the rapid aging in form-wound motor stators (Type II insulation) still requires clear understanding. Therefore, the proposed test method, along with the present results can be considered as a possible contribution for the further development of test standards and new techniques for the design of form-wound insulation of inverter fed motors.

1.5 Aim of the Present Work, and Thesis Organization

It has been demonstrated that the supply waveforms that are generated by the power converters play a major role in insulation degradation. Although, modern PWM converters have significantly reduced the harmonic distortions at low frequencies, the higher frequency harmonics has increased significantly. High frequency harmonics affect the voltage waveform with ringing and overshoots having amplitude, which depend on the supply-motor connection and commutation time of solid-state switches. In addition, the voltage drop is not uniform along the motor winding, being concentrated on the first few turns of a winding. Therefore, if PDIV is reached, even in a portion of the winding, PD activity that can be negligible under 60 Hz sinusoidal ac, can promote accelerated insulation degradation, especially in the presence of organic insulation (e.g., polyamide-imide based insulation).

The principal goal of this work is to promote a comprehensive understanding of the degradation processes of medium voltage form-wound stator coils that are exposed to various voltage waveforms. Medium voltage form-wound stator coils are selected since much of the previous work deals with low voltage (~1000V) random-wound motors fed by ASDs. A more in-depth knowledge of degradation mechanisms in form-wound stator coils provides a better understanding of the phenomena responsible for accelerated aging and a better direction in the design and manufacturing of new materials and insulation systems.

This research therefore focuses on a better understanding of the aging mechanism in form-wound coils under steep-front pulses. The main objectives of this thesis are listed below:

- A better understanding of the degradation phenomena in form-wound coils under steep-front voltage pulses.
- Contribution to the development of an accelerated aging test technique for form-wound insulation.
- A possible contribution to the development of new techniques for the designs of form-wound insulation for use on PWM-VSCs.

This thesis is organized as follows:

In Chapter 2, the preparation of the groundwall and turn insulation samples for this research is detailed. Also, the experimental setup and numerical analysis using FEM for the estimation of field distribution, due to space charge buildup, is described.

Chapter 3 presents the results of the long-term pulse aging test on groundwall insulation to determine its impact regarding the operating temperature range, pulse switching frequency, and voltages. In addition, the degradation mechanism of enamelled wires, subjected to different voltage waveforms, is examined. Since PWM drives exhibit significant harmonics and transients, the aging of test specimens, prepared by using enamelled wires, is accomplished by sinusoidal (60Hz), fast repetitive unipolar voltage pulses, and high frequency ac waveforms. The relation between the enamelled wire failure and the type of aging is also established by determining the residual dc strength. The thermally stimulated depolarization current (TSDC) technique is used to explain mechanisms such as charge injection and trapping, and to characterize the electrical behavior of the dielectrics under steep-front unipolar pulse voltage applications.

The analysis of results presented in Chapter 3, along with the examination of failed areas in the groundwall insulation, is discussed in Chapter 4. An empirical relationship between the relative release of the stored charge and aging time is additionally performed. Also, the performance of nanofillers for the suppression of PD in enamel wire coatings is included in the discussion.

Chapter 5 provides a summary and conclusions of the work on stator coil insulation systems studied. This last chapter also suggests some further work to improve the reliability of stator coil insulation system.

Chapter 2 Materials, Experimental Setup and Modelling

2.1 Introduction

In this chapter, the methods for preparing the samples for the turn and the groundwall insulation are described. For the turn insulation, in addition to the three commercial magnet wires, specially tailored nanofilled magnet wire specimens are also used. Both high frequency and steep-front pulses are adopted to age the specimens, and later, the residual life is determined by using the two-parameter Weibull distribution. To test the groundwall insulation, samples are prepared with a single layer of mica tape. To evaluate the performance of the groundwall insulation, the IEEE Std. 1043, 1553 [80,81], and IEC TS 60034-18-42, which is under development by IEC TC2 Working Group (WG) are followed [78]. To examine the space charge behaviour of the magnet wire coatings, the thermally stimulated depolarization current (TSDC) technique is employed. The experimental setup described in this chapter includes a high frequency ac and pulse aging circuit, thermovision system, PD measurement system, and imaging tool software. The software is applied to measure the surface roughness after capturing images using scanning electron microscopy (SEM).

2.2 Materials

2.2.1 Magnet Wire Base Material

The material used for the base coat for the magnet wires, relates to Pyre-ML® products, which belongs to the family of materials based on aromatic polyimides [82]. Pyre-ML® wire enamel RC-5019, which consists of polyamic acid; 13 wt% solution in NMP/aromatic hydrocarbon, is the most thermally stable organic material. It is essential

to note that RC-5019 does not contain any filler. The magnet wire base coat polyimide, after curing, can withstand high temperatures and is therefore used to protect motors, generators, transformers, and other apparatus, which operate continuously at temperatures up to 240 °C [82]. Also, Pyre-ML® protects heavy-duty motors which, due to a temporary extreme overload, acceleration torques, or stalls, are subjected to even higher temperatures (up to 400 °C) for limited periods of time. Some of the properties of Pyre-ML® RC-5019 are summarized in Table 2.1 [82,83]

Table 2.1: Polyimide (ML® RC-5019), magnet wire base material properties.

Property	Value
Viscosity	5000-7000 cps
Glass Transition Temperature	285 °C
Thermal Conductivity	0.12 W/m·K
Dielectric Strength	345 kV/mm
Dielectric Constant @ 1 MHz	3.2
Dissipation Factor @ 1 MHz	0.008

2.2.2 Nanofillers for Magnet Wire Overcoat

The proposed magnet wire specimens are built following NEMA MW-1000 specifications [84]. The first three layers consist of Pyre-ML® polyimide, are the base, on which the nanofilled insulation layer is applied. Three different types of nanofillers are selected for the overcoat. Their desirable characteristics for application in magnet wire insulation are highlighted below.

- Rutile Titanium Oxide, TiO₂

TiO₂ is useful as a filler to achieve a higher thermal conductivity and improved electrical properties. Since the heat stability improves significantly when it is used

with organic materials, nanoparticles of TiO_2 are promising candidates for the magnet wire coating. Table 2.2 lists typical values of some of the properties of interest [85].

Table 2.2: Properties of selected rutile titanium oxide, TiO_2 .

Property	Typical Value/Characteristic
Particle Size (nm)	54
Density (gm/cm^3)	4.2
Particle Appearance	Crystal Structure
Applications	Semiconductor materials, capacitors, pigments and coatings
Disadvantage	Not cost effective
Advantages	<ol style="list-style-type: none"> 1. Good dispersion 2. High resistance to PD 3. Improves dielectric withstand and voltage endurance characteristics 4. Mitigate space charge effects 5. Improves thermal properties

- Fumed Silica, SiO_2

Fumed silica is man-made silica of nano-size. It has desirable properties in terms high purity, extremely large surface area, and a characteristic to prevent slumping in coatings. Fumed silica has good thermal properties and imparts excellent mechanical and electrical characteristics to dielectric coatings. It can also be successfully used in a Pyre-ML® polyimide solution, a typical enamel wire coating. Consequently, in this work, the silica is chosen to improve the PD

resistant property of an enamelled wire. Table 2.3 reflects the typical values of some of the properties of the selected fumed silica, SiO₂ [86].

- Alumina, Al₂O₃

The nanoparticles of alumina (Al₂O₃) are selected due to its excellent dielectric and thermal properties. The reason for the selection of Al₂O₃ is to obtain a good comparison with the other two selected fillers by using the same concentration by wt% in the Pyre-ML® polyimide solution. The physical characteristics of alumina powder used in this work are given in Table 2.4 [87].

Table 2.3: Properties of selected fumed silica, SiO₂.

Property	Typical Value/Characteristic
Particle Size (nm)	32
Density (gm/cm ³)	2.2
Particle Appearance	Smoke-like
Applications	Rubbers and plastics, insulator coatings, batteries and abrasives, and sealants
Disadvantages	1. Difficult to get a good dispersion 2. Brittleness in coatings
Advantages	1. High resistance to PD 2. Prevents caking 3. Provide thickening 4. Improves dielectric strength

Table 2.4: Properties of selected alumina, Al₂O₃.

Property	Typical Value/Characteristic
Particle Size (nm)	62
Density (gm/cm ³)	3.2
Particle Appearance	Spherical
Applications	Outdoor insulation, HV insulator coatings, batteries and abrasives and thin film polymers
Disadvantages	<ol style="list-style-type: none"> 1. Comparatively less resistant to PD 2. Destroyed by acids 3. Brittleness in coatings
Advantages	<ol style="list-style-type: none"> 1. Excellent dielectric and thermal properties 2. Good resistance to tracking and erosion

2.2.3 Turn-to-Turn Specimens for Insulation Test

Wire Specimen Preparation

The wire specimens are built following NEMA MW-1000 specifications [84]. Three layers of Pyre-ML® polyimide are the base on which the nanofilled insulation layer is applied. The addition of a small amount, 1 to 5 wt%, of inorganic nanofillers, is sufficient for performance improvement [88], and a higher concentration can cause the coating to become more brittle. Therefore, the nanofillers, ~1 % by weight, are used in standard polyimide enamel.

To prepare the nanofilled layers, the nanofillers and the polyimide base material are first weighed and then mixed in a blender. The material is degassed in a vacuum chamber, and applied to a magnet wire, having rectangular shape with smooth and continuous corner, bearing a width of 7.09 mm, and a thickness of 2.82 mm. After the material is cured in an oven for 2 hours at 90-100 °C, the uniformity of the filler

dispersion is checked by using a SEM with an energy dispersive x-ray (EDAX) attachment. The cross section of magnet wire specimen used for experimental investigations, is displayed in Figure 2.1.

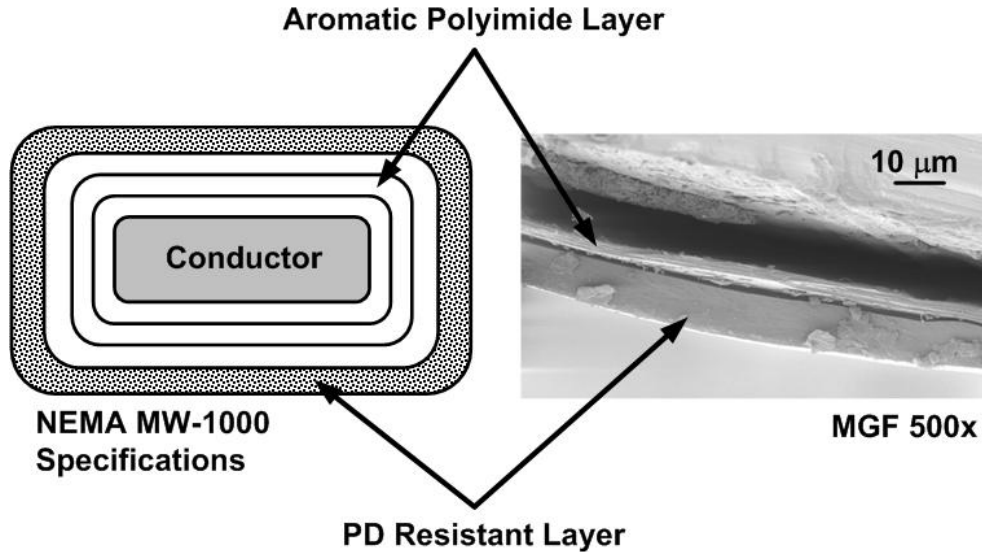


Figure 2.1: Cross section of magnet wire showing coating layer.

Table 2.5 summarizes the characteristics of the conventional (S_1 , S_2 , and S_3) and newly developed enamelled wires (S_4 , S_5 and S_6). The coating on S_1 is achieved by a Pyre-ML® solution that is aromatic polyimide-based; whereas, S_2 and S_3 are PD resistant. Enamelled wires S_4 , S_5 , and S_6 , developed in the laboratory, also belong to the family of PD resistant wires and have an additional coating of filled fumed silica (SiO_2), TiO_2 , and Al_2O_3 , respectively.

Table 2.5: Parameter related to magnet wire.

Magnet Wire	Coating Type on Magnet Wire	Coating Thickness (μm)	DC Dielectric Strength (V/m) $\times 10^7$	PDIV_p (kV)
S ₁	Pyre-ML® Polyimide	38	29.0	0.92
S ₂	Corona Resistant MGF	25	31.0	1.28
S ₃	Kapton FCR	41	29.0	1.70
S ₄	Pyre-ML® Solution + SiO ₂	28	27.0	1.15
S ₅	Pyre-ML® Solution + TiO ₂	24	29.0	1.05
S ₆	Pyre-ML® Solution + Al ₂ O ₃	27	25.0	0.98

Sample for Inter-Turn Evaluation

The type of testing necessary to evaluate the inter-turn insulation for inverter duty motors is not standardized; as a result, based on form-wound coil geometry, the turn-to-turn samples are prepared, as shown in Figure 2.2. These geometries (both type A & B), which are similar in configuration, based on the stator coil design. Here, the square or rectangular magnet wires are arranged in a parallel fashion to achieve a single turn. As shown in Figure 2.2, plastic sheets are used instead of metallic ones to avoid external damage to the magnet wire coating and to keep the stress uniform between the two turns.

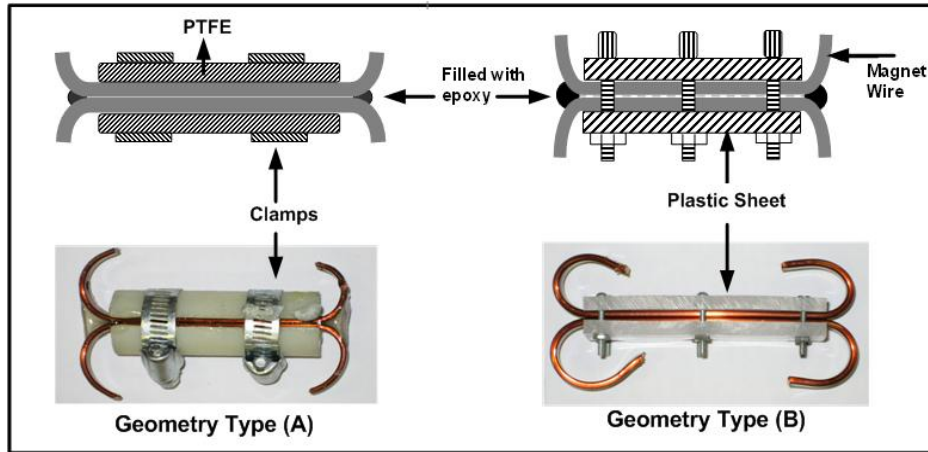


Figure 2.2: Turn-to-turn samples geometry.

2.2.4 Preparation of the Samples for the Groundwall Testing

The VPI stator bar samples received from the manufacturer rated at $\sim 1.5 \text{ kV}_{L-L}$ are wound with only one layer of the groundwall mica-paper tape. The samples are used for different types of accelerated aging tests. In this research, 42 stator bar samples are used. As a reference, the samples are serially marked. To reduce the capacitive load on the test supply, a reduced sample size of $\sim 51 \text{ cm}$ in length is chosen. Figure 2.3 depicts these VPI stator bars along with their specifications.

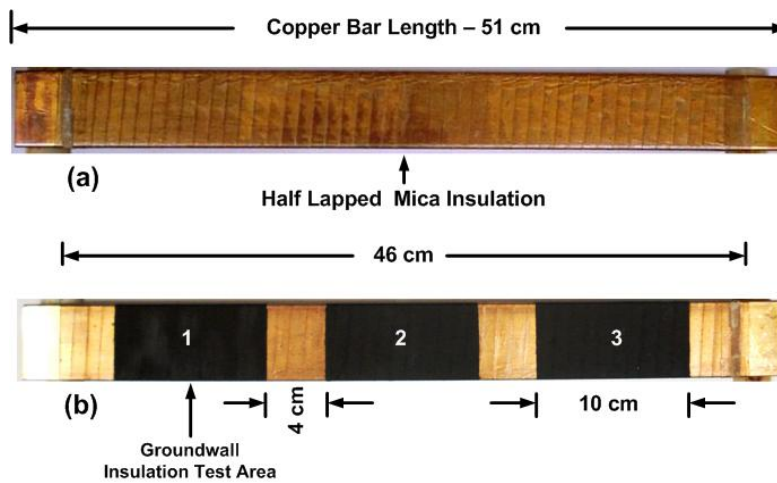


Figure 2.3: VPI stator bars with single layer of mica flakes tape (a) bars received from manufacturer, (b) divided into three test areas.

In Figure 2.3, each test area marked as 1 to 3 has further six-layer geometry. The six-layer geometry has several advantages and is depicted in Figure 2.4. A graphite loaded conductive coating in the form of paint is applied as layer 2 to the stator bar specimens, along with a stress grading layer 3, which prevents PD from occurring at the end of the conductive paint. Aluminum foil (layer 4) is used as a ground plate and for uniform heat distribution, when the heat is applied. The purpose of layer 5 is to fill the gaps at the edges of the foil and to precisely record the thermal profiles by using the infrared camera. In addition, the black conductive layer helps to correct the emissivity, which is adjusted to 0.92 in this experiment. Outer layer 6, like layer 3, consists of stress coating. This prevents any further PD from occurring at the end of aluminum foil and to avoid stresses that are concentrated near the ends during the high frequency pulse voltages.

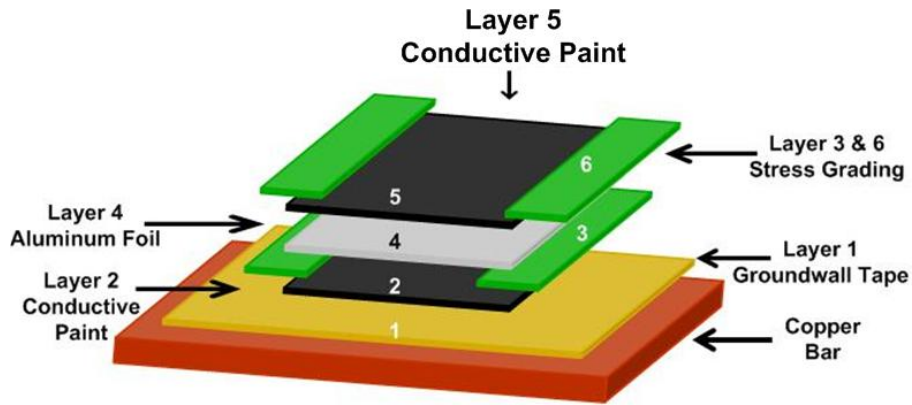


Figure 2.4: A six-layer system for evaluation of groundwall insulation.

2.3 Statistical Analysis

In the breakdown testing of the solid dielectric insulation and in reliability studies, scatter appears in the data, even within a fixed set of test conditions. Such variability is normal of life data. Moreover, substantial research has been done on how to analyze such data to extract the significant conclusion from the midst of the inherent variability. To summarize the data, statistical techniques are applied, such that, each set of recorded data is represented by a mean and standard deviation. The two most common statistical

distributions for analysis are the Weibull distribution and the Lognormal distribution [89].

In this thesis, a group of 15 enamelled wires that belong to the same class are aged. Therefore, the Weibull distribution, which is a version of the Extreme Value group of distributions, is applied for the measurement of dc breakdown strength. Considering the breakdown strength, E as the random variable, the cumulative Weibull distribution may be written, in its general form, as:

$$F(E) = 1 - \exp\left[-\left(\frac{E - E_{\min}}{\eta}\right)^\beta\right]; E_{\min} < E < \infty, \quad (2.1)$$

$$\beta, \eta > 0$$

where E is the electric field in V/m. The parameter η represents the magnitude of E for failure of 63.2% tested units. Similarly, parameter β , which is also called the “shape parameter”, is a measure of the dispersion of E . Parameter E_{\min} , which is referred to as the threshold parameter (V/m), is that value of E , below which, breakdown is not possible. In order to plot the data on probability paper, it is necessary to rank them and assign cumulative probability failure, F , to each point. A calculation of F depends on the ranking scheme such as the median and mean ranking. The median ranking is given by:

$$F(i, n) = \frac{i - 0.3}{n + 0.4} \quad (2.2)$$

where the mean rank approximation is:

$$F(i, n) = \frac{i}{n + 1} \quad (2.3)$$

In Equations (2.2) and (2.3), n is the recorded breakdown times or voltages in order from smallest to largest, which are ranked from $i = 1$ to n . Although, the mean rank function is recommended by IEEE Std. 930, the median rank is shown to be more appropriate [89,90,91].

2.3.1 Weibull Analysis

In predicting the equipment life, the Weibull analysis is well developed [48]. Usually, the shape and scale parameters are estimated by the method of Maximum Likelihood Estimation (MLE) [92]. Statistically, the MLE is considered to be robust and yields estimators with good statistical properties. By considering Equation (2.1), the likelihood function is defined by [93,94,95,96]:

$$L(E_1, E_2, \dots, E_N | \bar{\eta}, \bar{\beta}) = L = \prod_{i=1}^N f(E_i; \bar{\eta}, \bar{\beta}) = \prod_{i=1}^N \frac{\bar{\beta}}{\bar{\eta}} \left(\frac{E_i}{\bar{\eta}} \right)^{\bar{\beta}-1} \exp \left[- \left(\frac{E_i}{\bar{\eta}} \right)^{\bar{\beta}} \right] \quad (2.4)$$

The logarithmic likelihood function is given by:

$$A = \ln L = \sum_{i=1}^N \ln f(E_i; \bar{\eta}, \bar{\beta}) = \sum_{i=1}^N \ln \left[\frac{\bar{\beta}}{\bar{\eta}} \left(\frac{E_i}{\bar{\eta}} \right)^{\bar{\beta}-1} \exp \left[- \left(\frac{E_i}{\bar{\eta}} \right)^{\bar{\beta}} \right] \right] \quad (2.5)$$

The ML estimators $(\bar{\eta}, \bar{\beta})$ are determined by taking the partial derivatives of A , with respect to $\bar{\eta}$ and $\bar{\beta}$, and setting them to zero; i.e., $\frac{\partial A}{\partial \bar{\eta}} = 0, \frac{\partial A}{\partial \bar{\beta}} = 0$. By solving Equation

(2.5), best estimates $\bar{\beta}$ and $\bar{\eta}$ are:

$$\frac{1}{\bar{\beta}} = -\frac{1}{N} \sum_{i=1}^N \ln E_i + \frac{\sum_{i=1}^N \ln(E_i)^{\bar{\beta}} \ln E_i}{\sum_{i=1}^N \ln(E_i)^{\bar{\beta}}} \quad (2.6)$$

and

$$\bar{\eta} = \left[\frac{1}{N} \left(\sum_{i=1}^N (E_i)^{\bar{\beta}} \right) \right]^{\left(\frac{1}{\bar{\beta}} \right)} \quad (2.7)$$

Equation (2.6) is written in terms of $\bar{\beta}$ only, and is solved by an iterative technique such as the Newton-Raphson iterative technique. Once $\bar{\beta}$ is obtained, $\bar{\eta}$ can be determined by using Equation (2.7). Although the methodology for the MLE is simple, the implementation is mathematically complex [97]. In this work, a specialized package, WinSmith Weibull software, is used to find the ML estimates of the Weibull distribution parameters [98].

2.4 Modelling of Systems with Inter-turn Stress

The modelling of the inter-turn insulation to identify the stresses is an essential tool in the design and optimization of such systems. An accurate model can be applied to do the following [99,100]:

- To describe how the system is likely to behave under particular conditions,
- To modify the material characteristics to fit specific requirements;
- To predict the effects of aging and determine the material's lifetime in order to establish a maintenance policy.

Typically, problems with magnet wire coating systems can be represented with the subdomains of the conductors, subdomains of perfect dielectrics (air or another surrounding medium and main coating insulation). Conductors are considered to be perfect conducting regions of known potential.

For a region with the coating materials, the first Maxwell equation (Ampere's law) states that:

$$\nabla \times H = J + \frac{\partial D}{\partial t} \quad (2.8)$$

J is the conduction current density and $\frac{\partial D}{\partial t}$ is the displacement current density.

By applying the divergence to both sides of Equation (2.8),

$$\nabla \cdot \nabla \times H = \nabla \cdot [J + \frac{\partial D}{\partial t}] = 0$$

or

$$\nabla \cdot [J + \frac{\partial D}{\partial t}] = 0 \quad (2.9)$$

Equation (2.8) is known as the continuity equation, where

$$J = \sigma_{DC} E + D,$$

$$D = \epsilon_o E + P,$$

where P is the remanent polarization, which is the displacement when no electric field is present, and E is:

$$E = -\nabla V$$

In the above equations, σ is the electrical conductivity and ϵ_0 is the vacuum permittivity [101]. In this thesis, the above equations are solved, by considering σ as a constant, because the main conduction mechanism in polyimide is the Ohmic, which remains stable in a wide range of electric field [102]. The surrounding media is assumed to be perfect, linear, and isotropic dielectrics. The equations for each subdomain are combined by boundary conditions [103], and solved analytically or numerically. FEM (finite element method) [104] Finite Differences [105], or an Equivalent Circuit Model [99] can be used for this purpose. In this research, FEM is used to model the field distribution in the inter-turn insulation due to some advantages it has, for example, over the equivalent circuits models. More details on the inter-turn model for verifying the electric field stress are found in Appendix A.

2.4.1 Finite Element Method (FEM)

The FEM approximates the solution to the partial differential equations in a domain, composed of a mesh of elements whose vertices are called nodes. FEM, applied to any problem, is defined in four steps [106] as follows:

- Step 1: Discretize the solution region in a finite number of subregions named elements.
- Step 2: Define the equations that describe a typical element.
- Step 3: Combine all the elements in the solution region.
- Step 4: Solve the system of equations obtained.

In the FEM, the potential distribution in a volume is defined by the principle of minimum energy [107]. In this case, the electrical energy over the domain Ω , is given by as follows [108,109]:

$$W = \int_{\Omega} \frac{1}{2} (\sigma + \varepsilon \frac{\partial}{\partial t}) E \cdot E d\Omega \quad (2.10)$$

or, in the frequency domain, as:

$$W = \int_{\Omega} \frac{1}{2} (\sigma + j\omega \varepsilon) E \cdot E d\Omega \quad (2.11)$$

In the FEM, the functional, given by Equation (2.9), is discretized and formulated as a function of the nodal potentials, and then minimized to give the voltage distribution [109,110].

In the present work, FEMLAB[®] version 3.3, a finite element software, is used to compute the electric field between the polymer interfaces. FEMLAB[®] can directly solve the problems, described by Equation (2.10) and Equation (2.11).

2.5 Characterization of Stored Charge in Solid Dielectrics

Solid dielectric materials may store charges, when subjected to external electric field. In highly resistive materials, such as polyethylene and polyimide, space charges, usually, accumulate near the electrode. These stored charges move out of the sample under the short circuit conditions with the assistance of the thermal motions of the molecule, leading to a current in the external circuit. Various mathematical models and experimental techniques are now available to study charge trapping and its release in solid dielectrics [111,112].

Thermally stimulated depolarization current (TSDC) is one of the techniques that is available to investigate the electrical properties and charge storage mechanisms in dielectrics. Before initiating TSDC measurements, specimens of enamelled wire S₁ and S₂ were sent to TECHIMP in Bologna, Italy, to confirm the existence of space charge build up by using pulsed electroacoustic (PEA) technique. Excessive charge trapping was observed in both types of specimens, for which, the results are reported in appendix B.

Once the charge trapping is confirmed, TSDC method was adopted for different type

of magnet wire samples during the course of this investigation. In TSDC measurements, it is additionally possible to confirm the contribution of more than one factor that can contribute to the measured current. The magnitude of the current, which is affected by the disorientation of the dipoles [111], is determined by the charge liberated from the traps. The existence of this current is explained by the movement of the de-trapped charge in the field that is determined by the accumulated charges [112]. The motion of the molecules, which substantially increases with higher temperatures facilitates the movement of the charges and determines the increase in the current and is commonly known as the temperature-dependent component of the current. The experimental conditions are selected so that the time-dependent component can be neglected in certain cases, and the analysis can be carried out as a function of the temperature.

2.5.1 Thermally Stimulated Depolarization Current (TSDC) Method

The TSDC method is based on the depolarization of a sample by thermal activation. The depolarization current, when the temperature is increased at a constant rate, exhibits a series of maxima, which correspond to the different thermal transitions. In this technique, which is also known as the temperature-dependent TSDC method, the sample is polarized by externally applied electric field, E_p , at temperature, T_p . Polling time, t_p , which varies and is much longer than the relaxation time, models the aging period of the specimen. Subsequently, this polarization is frozen-in by cooling the sample in the presence of the applied electric field to room temperature such that the frozen-in polarization remains unchanged, even if the external field is switched off. By heating the sample at a constant rate, the depolarization current, as the polarizing specimens relax, is detected by a high sensitive electrometer. For dipoles with a single relaxation time, the decay of the polarization, due to the disorientation of the dipoles following the removal of the electric field at $t = 0$ and temperature T is given by Bucci *et al.* [113]. The authors developed a complete theory to account for the dipolar reorientation. During the TSDC measurements the dipoles reorient on reheating the dielectric and the rate at which the instantaneous

polarization P decays with time can be expressed in terms of the polarization and relaxation time τ by:

$$\frac{dP}{dt} = \frac{-P}{\tau(T)} \quad (2.12)$$

and the solution to Equation (2.12) is:

$$P(t) = P(0) \exp\left[\frac{-t}{\tau(T)}\right] \quad (2.13)$$

where $P(0)$ is the “frozen-in” steady state polarization at $t = 0$, and $\tau(T)$ is the relaxation time, which is characteristic of the frequency jumps of the dipole and is given by the Arrhenius relationship:

$$\tau(T) = \tau_o \exp\left(\frac{-\varepsilon_a}{kT}\right) \quad (2.14)$$

where τ_o^{-1} is the characteristic frequency factor, ε_a is the activation energy of dipolar orientation, and k is Boltzmann’s constant. By assuming a linear increase in temperature, from low value T_o , at rate x (where $T = T_o + xt$), the non-isothermal equation for the polarization decay is:

$$P(t) = P(0) \exp\left(-\int_0^t \frac{dt}{\tau(T)}\right) \quad (2.15)$$

Therefore, the current density j , generated by the decay in polarization is simply the rate of change of polarization and expressed by:

$$j(T) = -\left(\frac{P(0)}{\tau}\right) \exp\left(-\int_0^t \frac{dt}{\tau(T)}\right) \quad (2.16)$$

Combining Equations (2.14), (2.15) and (2.16) corresponding to depolarization,

$$j(T) = -\left[\frac{P(0)}{\tau_o}\right] \exp\left(\frac{-\varepsilon_a}{kT}\right) \exp\left(-\frac{1}{x\tau_o} \int_{T_o}^T \exp\left(\frac{-\varepsilon_a}{kT'}\right) dT'\right) \quad (2.17)$$

As described, $P(0)$ is the level of polarization, which is ‘frozen-in’ at temperature T_o . In a TSDC experiment the initial polarization is performed at a high temperature T_p and the specimen is then cooled to T_o [114].

2.5.2 Stored Charge and Trapping Levels

The electron traps have various energy and density [115], especially for wire coatings. The charge storage in a dielectric and its release from different trap levels are estimated by utilizing the TSDC plots. By modifying equation (2.15), the charge remaining in the sample is computed as:

$$Q = \int_{t(T)}^{\infty} j(T) dt \quad (2.18)$$

and the relaxation time is

$$\tau = \left(\frac{Q}{j} \right) \quad (2.19)$$

From (2.13),

$$\ln \tau(T) = \ln \tau_o + \frac{\epsilon_a}{kT} \quad (2.20)$$

The plot of $\ln \tau(T)$ versus $1/T$ yields a straight line with slope ϵ_a , which determines the activation energy for the charge carriers [116]. Trap levels, which have discrete energy differences, can be identified by a distinct peak in the thermogram by using TSDC plots.

2.6 Experimental Setup

The following sections describe the setups used in the experimental work. The arrangements for the PD measurements under pulse, the temperature measurement system, and the setup for the measurement TSDC are described. In addition, the pulse and high frequency ac aging circuits are also described in the following sections.

2.6.1 PD Measurements

Electrical Detection Method

In the electrical detection method, to measure the PDIV, a device called the XTrac™ is adopted to identify the existence of PD from a surge pulse. The instrument is capable of measuring, on three channels; the PD activity of the PWM operated machinery [117]. The first two channels are rated for an input voltage as high as 5 kV_p; whereas, a third channel is rated for 10 kV_p. The unit contains PD detection along with noise filtering capabilities. The unit is installed between the pulse generator and the test bar for all the measurements. The overall electrical connection of the instrument for the PD detection is shown in Figure 2.5.

The detectable PD signal is accessible on the front panel as a low voltage signal that is displayed on an oscilloscope. For reference, the system output voltage, which is applied to the terminals of the test samples, is measured with a high voltage Tektronix probe. This probe is capable of measuring a peak voltage of 20 kV, and its output is also a low voltage signal that is displayed on the same oscilloscope. The digital oscilloscope has a 400 MHz bandwidth, four channels, and a storage capability.

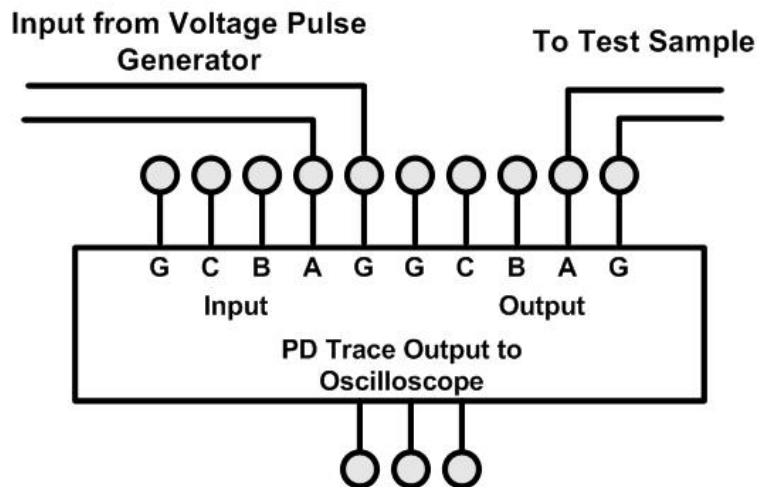


Figure 2.5: Electrical Connection for PD measurement using XTrac™ [117].

The measurement of PD under fast rise time voltage waveforms is difficult, since the frequency ranges of the rising voltage and PD signals almost overlap. In such cases, an

effective filtering is difficult and requires special tuning. But XTrac™ has special features for the efficient filtering of noise with a predominant PD signal. To determine the PDIV in the VPI stator bar specimens, the test voltage is applied gradually, until PD is observed. A typical PD signal, detected by using the electrical detector, is shown in Figure 2.6 [117].

In all the waveforms recorded through XTrac™, the surge remnant, which can be easily distinguished from the PD pulses, is ignored which comes through the detector. The high frequency output from the detector indicates PD signals, which has a rise time between 5-10 ns.

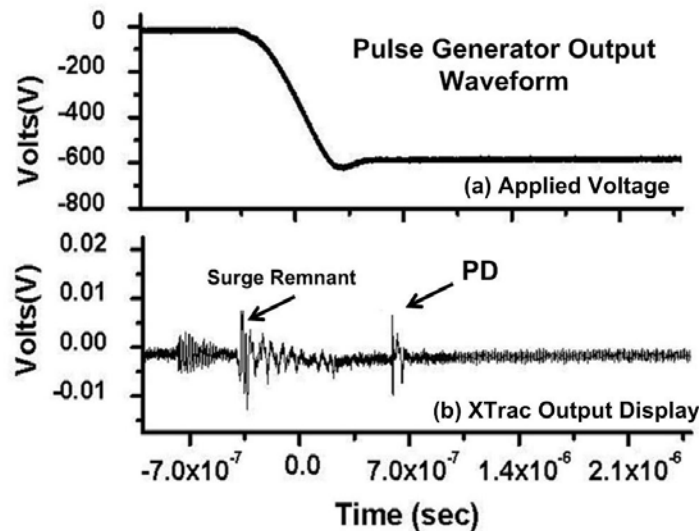


Figure 2.6: An example of the oscilloscope trace of a PD signal, along with the output voltage waveform from the detector.

Optical Detection Method

The daylight CoroSMART camera that belongs to CoroCAM's family of ultraviolet and bi-spectral cameras is used to visually locate the source of the electrical corona or arcing. The camera is low-light, UV filtered, very portable, battery powered, and rugged has an ultraviolet viewer to observe the electrical corona on switchgears, electric motor windings, low-light levels, and for outdoor substations between dusk and daybreak, and

many other applications. The camera is chosen for the test because of the need to reference and calibrate the electrical PD detection.

Figure 2.7 shows the images of twisted pairs recorded by using CoroSMART camera. The PDIV level, recorded with the electrical PD detector, demonstrate a value of 1.9 kV_p ; whereas, the discharge activity, observed with an optical detector is approximately 2.05 kV_p . The XTracTM is calibrated for $\pm 7\%$ error, accordingly, for all the measurements during this investigation.

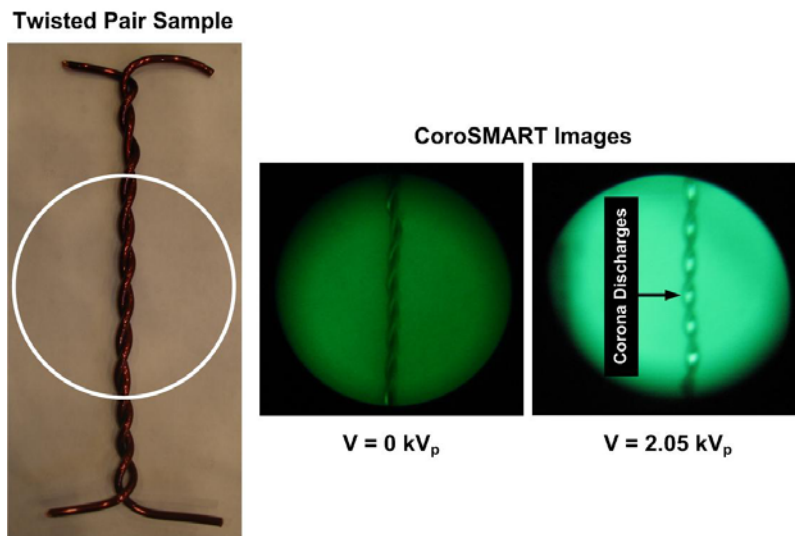


Figure 2.7: Image recorded using CoroSMART Camera (optical detector) with corona discharge activity.

2.6.2 Temperature Measurements using an Infrared Camera

The temperature measuring system consists of an infrared camera and thermovision acquisition software. The system consists of a FLIR-SC500 infrared camera with an emissivity spectrum between 7.5 and $13 \mu\text{m}$ that displays the temperature image in a 320×240 pixel array, Figure 2.8. The sensitivity of the detector is 0.07 K at a temperature of 303 K and with an accuracy of 2 K over the range 273 to 773 K . The acquisition software, ThermaCAMTM Researcher, allows different types of post-processing of the temperature distribution in the infrared image. The emissivity is adjusted to 0.92 for the

groundwall stator bar samples. The emissivity calibration is conducted on the samples, which are in an oven at 313 K (40 °C) using the temperature measured with a thermocouple as a reference. Figure 2.9 depicts the measured profile of temperature, T , on the surface of a 4 kV form-wound stator coil. The pulse voltage applied was 2.5 kV_p at a switching of 2000 pulses per second (pps).

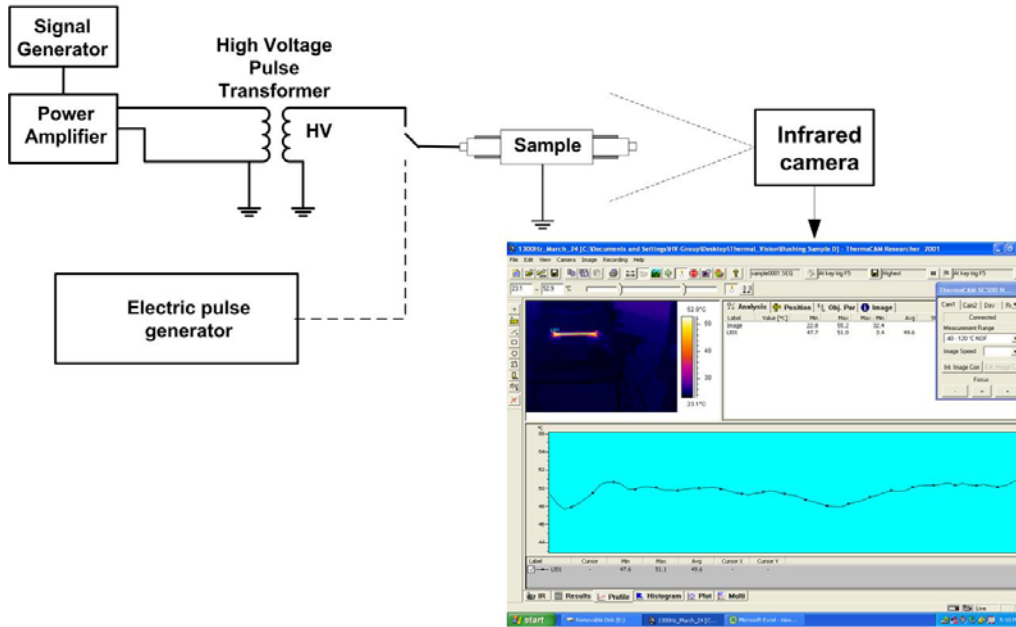


Figure 2.8: Temperature measurement system [118].

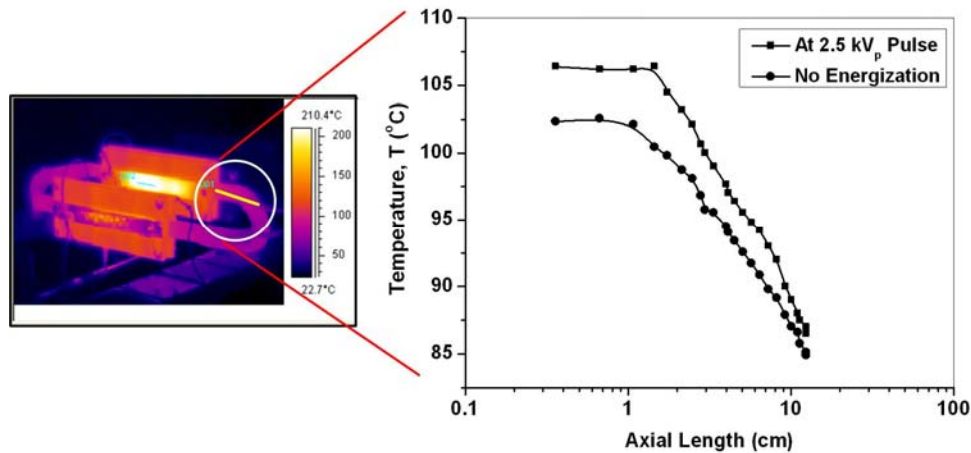


Figure 2.9: Measured temperature on the surface of the 4.0 kV_{L-L} form-wound stator coil energized at 2.5 kV peak ($f_s = 2$ kHz).

2.6.3 Measurement of the TSDC

Figure 2.10 shows the schematic of an experimental arrangement for the study of TSDC. The temperature of the specimen is controlled using an environmental chamber, which is controlled by a microprocessor unit designed to operate over a temperature range of -80 to 200 °C. The temperature control and measurement is accurate to 0.1 °C. The specimen under test is aged by different types of voltage waveforms for different durations and the current is later recorded.

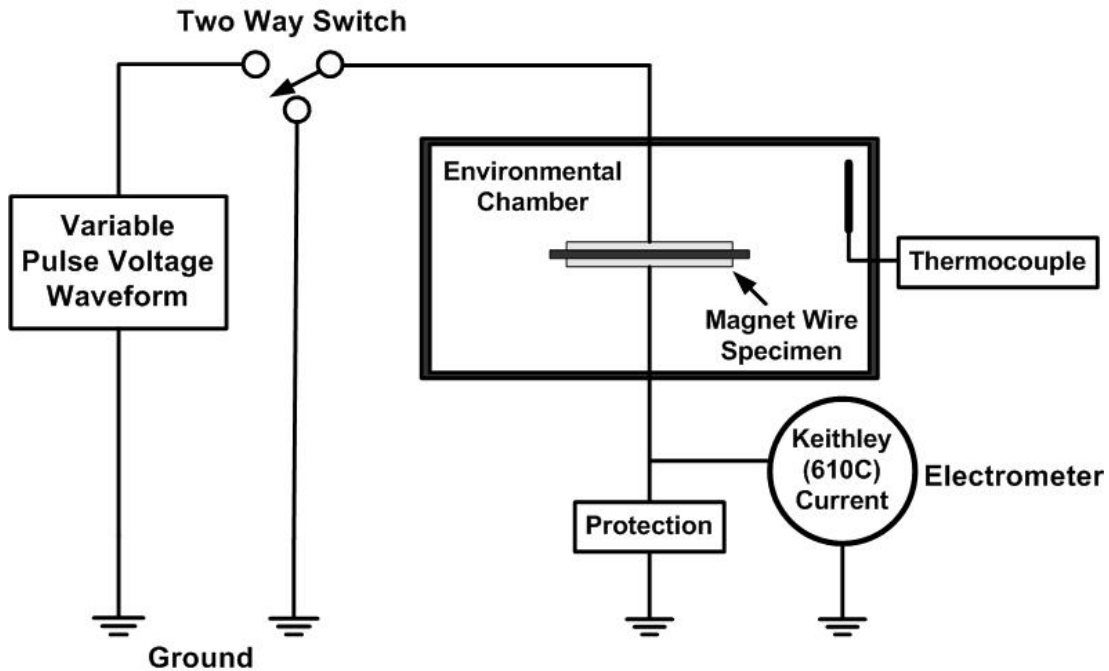


Figure 2.10: Schematic of an experimental arrangement for the study of TSDC.

Many small bar specimens, shown in Figure 2.2, prepared with enamelled wires, that belong to the insulation class F (155 °C), are adopted for all the TSDC experiments. Since the test specimens are partially dried and might contain moisture, the reproducibility of the currents is improved by adopting the thermal protocol in Figure 2.11. The environmental chamber, in which the test specimen is placed, is heated up to 200 °C (A-B), and the temperature is held constant for three hours (B-C). At the end of this period, the chamber temperature is lowered to the desired temperature of 155 °C (D-E), where the specimen is aged by different types of voltage waveforms for different

durations. After the aging, the temperature is decreased to 23 °C, and the sample is kept short-circuited for 30 min (F-G). Finally, the TSDC measurements (G-H) are carried out by using a Keithley 610C electrometer and a temperature controller [119]. Both the heating and polling of the test specimens are carried out under normal pressure.

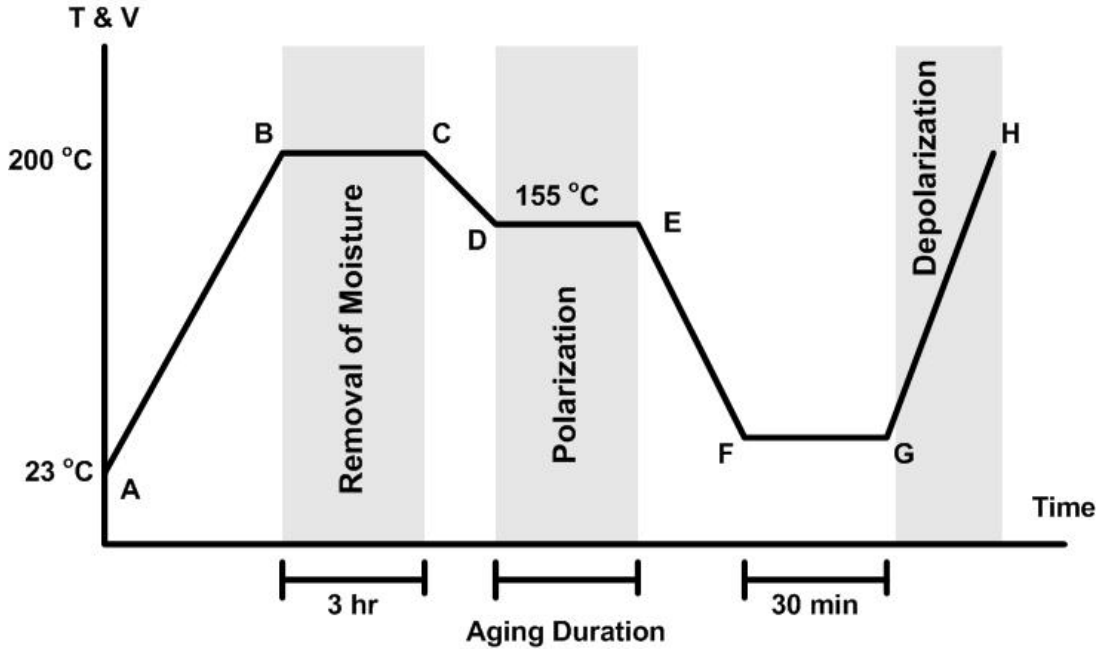


Figure 2.11: Thermal protocol and steps for the measurement of TSDC. [119].

The TSDC current, recorded as a function of the temperature, is easily converted to the function time for the measurement of the stored charge released, as the temperature is increased linearly. The conversion of the temperature to the time scale is achieved by following equation:

$$T = T_o + xt \quad (2.21)$$

where T is the temperature of the sample; T_o , the initial temperature; x , the heating rate; and t , the time. A typical TSDC plot for both low and high temperature polymers is shown in Figure 2.12. In low temperature polymers, the TSDC measurements could be extended up to a temperature at which the current vanishes. This is usually the glass transition temperature, T_g . At this temperature no more charge is released to the external circuit [116].

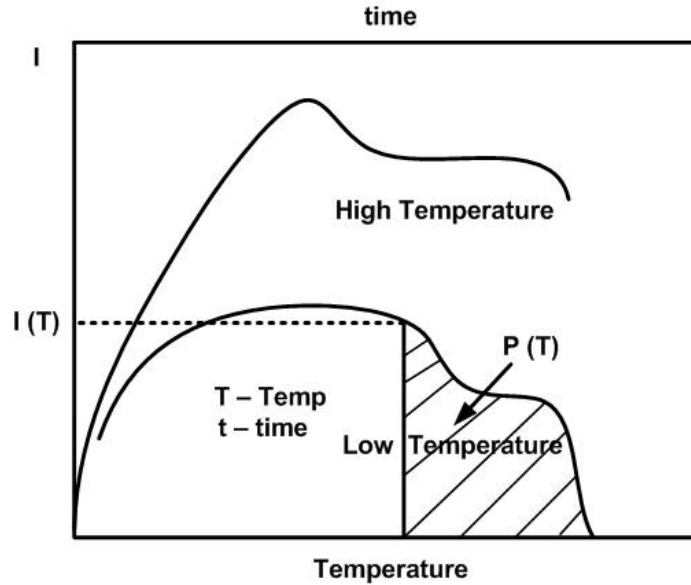


Figure 2.12: Schematic of TSDC in polymers.

2.6.4 Pulse Aging Test Circuit

Pulse Voltage Generator

To perform the long-term aging tests on both the magnet wire specimens and groundwall stator bar samples, a high voltage pulse modulator (HVPM), developed by DTI is used [120]. The HVPM, illustrated in Figure 2.13, is capable of providing the voltages that result from medium voltage (2.3-6.6 kV) PWM drives. The 30kV-30A voltage source modulator is built with solid-state switches in series, providing a high peak power and constant voltage during each pulse. Additionally, the modulator system contains a dc power supply, and a function generator. A variable voltage of 0 to 30 kV is provided by the dc power supply with a limit for the continuous operation of 540 mA. The voltage is varied by a dial indicator on the front panel. A standard function generator is used to generate the gate signals from the TTL output for the IGBT switch module. Switching frequency (f_s) of the output pulse voltage waveform can be varied up to 10 kHz by using the function generator.

According to IEC 62068 [121], simple voltage waveforms, either bipolar or unipolar, can be adopted for testing the insulation system objects and comparing their behaviour

with respect to reference assessed insulation systems [122]; therefore, a steep-front unipolar pulse is selected. Based on the latest developments and information available in the literature, most of the modern converter output voltage rise times fall in the 50–2000 ns range due to the power semiconductor switching characteristics [78,103,123]. In view of this information, a pulse rise time of 400 ns and a maximum switching frequency as high as 3 kHz are selected for the insulation aging.

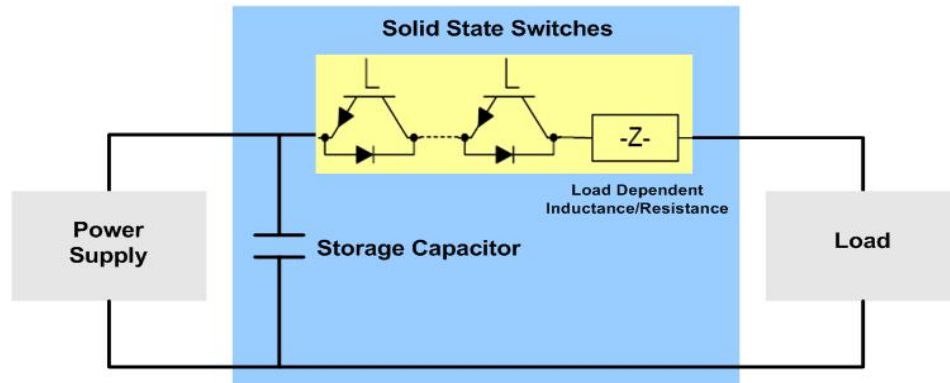


Figure 2.13: High voltage pulse modulator used for endurance test [120].

Test Procedure

The aging experiments are carried out under different pulse amplitudes and frequencies, and for different values of test temperatures using schematic shown in Figure 2.14 [124]. To determine the lifetime of an insulation sample, the time is measured until a puncture in the insulation occurs. Electrical and thermal aging deteriorates the insulation such that a hole is eroded through the insulation, and the copper in the bar shorts to the ground plate. Thus, the mean time-to-failure is a direct measure of the duration for which the test voltage is applied, before the power supply automatically turns off [4]. The accelerated aging conditions, to understand the degradation processes, are reported in Table 2.6.

The techniques for accelerated voltage aging are also described in IEC 62068-1 [121] and IEC 60034-18-32 [125]. They are based on a comparison of the life tests, performed on the candidate system and on the reference system, previously assessed for its service life, in which voltage endurance coefficient, n , is defined by the following lifetime equation:

$$D = kV^{-n} \quad (2.22)$$

Here, characteristic life, D , is related to the applied test voltage by using the inverse power law, and k is a constant that depends on the material and applied test voltage [78]. In particular, the values of constant, n , are likely to be different for the different breakdown mechanisms, operative at different applied voltages. Therefore, it might not be valid to estimate the aforementioned parameters in the test voltage range, which are very high, in order to estimate the expected lifetime. However, this technique requires further testing at three or more over-voltages and frequencies, summarized in Table 2.6. This allows the calculation of the voltage endurance coefficient from the regression line by the linear regression technique, applied to $(\log \alpha, \log V)$, the transformation, and any life at a generic percentile for a selected voltage [78].

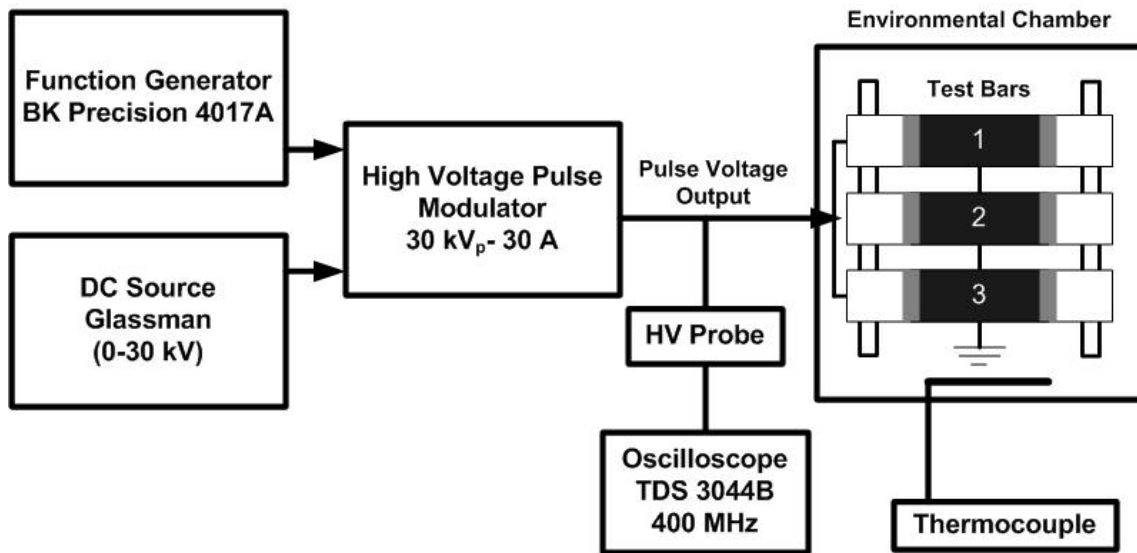


Figure 2.14: Schematic representation of circuit employed for pulse endurance test.

Table 2.6: Test conditions for groundwall aging.

Test Voltage Levels (V_p)	Voltage Waveform Frequency	Temperature ($^{\circ}C$)
4000, 5000, 6000	500, 1500, 3000 Hz pulses	20, 120, 155
4000, 5000, 6000	60 Hz ac waveform	20, 120, 155

As depicted in Figure 2.15, to acquire the temperature of 120 °C and 155 °C, a rope heater is wrapped over the aluminum foil for heating the groundwall insulation; whereas for the tests at room and below room temperatures, an environmental chamber is used, as shown previously in Figure 2.14.

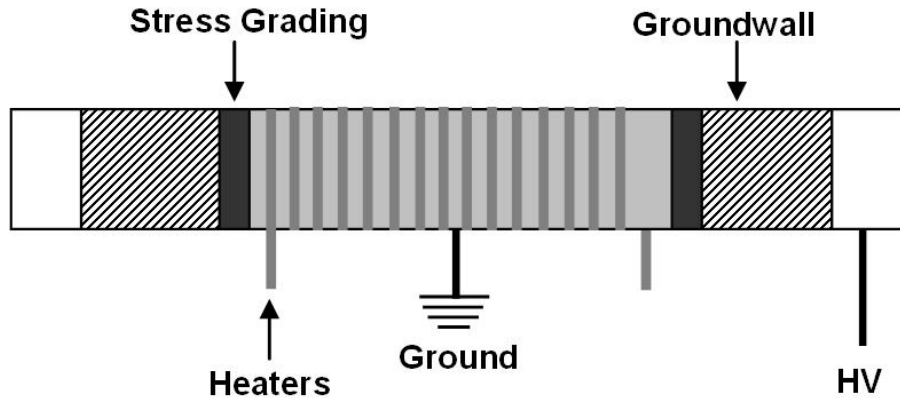


Figure 2.15: Stator bar specimens used for evaluation at high temperatures.

2.6.5 High Frequency AC Test Setup for the Aging of Magnet Wire Coatings

Choice of High Frequency AC Waveforms

The spectrum analysis of the PWM waveforms reflects a wide range of harmonic components. Although these high frequency harmonics exhibit a low-voltage amplitude and low-energy content, they can cause stress on the stator winding insulation due to high wavefronts (dV/dt). These harmonics can excite local resonance, causing voltage harmonics with a high amplitude. Often a filter is used in low voltage applications to absorb the standing waves, but at higher voltages, filters are not used.

The analysis of the spectra, obtained from a real drive with dominating harmonics between 3-4 kHz, is depicted in Figure 2.16. Modern IGBT-based ASDs have modulation frequencies in the range of 0.5 kHz to 20 kHz with rise times of 50–2000 ns. The spectrum of ASDs has an output frequency, close to the modulation frequency with a substantial power content as high as the sixth harmonic of the modulation frequency.

From this information and for accelerated aging, wide range of frequencies from 60 Hz to 10 kHz is selected for all the tests on the enamelled wires.

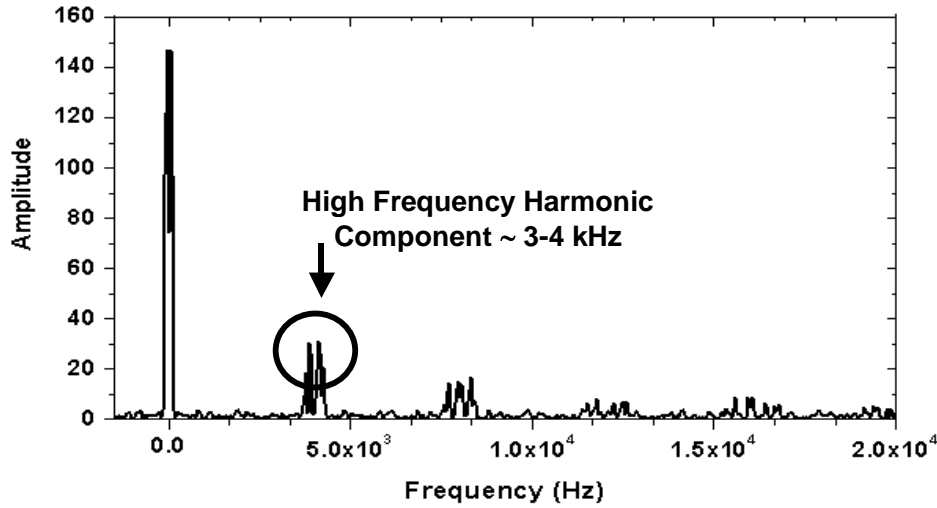


Figure 2.16: FFT spectrum of the PWM drive (Modulation frequency: 3-4 kHz).

High Frequency AC Endurance Test Circuit

For the magnet wire enamel evaluations, a voltage endurance test circuit with a high frequency voltage of a sine-wave power supply, is additionally adopted. In the test setup, as depicted in Figure 2.17, a high frequency generator produces a sinusoidal voltage signal that passes through an audio amplifier, and a high frequency step-up transformer (50V/20kV), which ages the samples. To identify the voltage across each test sample, a digital oscilloscope is used. Also, the same test circuit is employed for the PD erosion test to observe the surface roughness, which is described later in Section 2.6.5.

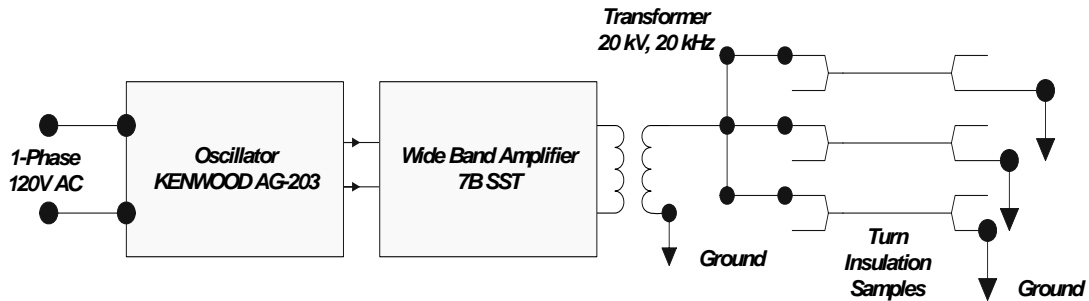


Figure 2.17: High frequency test voltage source.

Determination of Residual Insulation Strength

The most common and acceptable test for determining the breakdown strength of enamelled wire insulation is to use a dc test. The dc breakdown voltage experiment had shown that there is no significant difference between positive and negative polarity voltages, indicating that the field is nearly uniform between the two turns [126]. In both aged and un-aged specimens a group of 15 enamelled wires that belong to the same class are used. The experimental data, for both aged and un-aged samples, is then analyzed by using a two-parameter Weibull distribution to establish the scale and shape parameters, as described in Section 2.3.1. The scale parameter represents the time (or voltage) for which the failure probability is 63.2%. Similarly, the shape parameter, β , is a measure of the range of the failure times or voltages. The larger is the value of shape parameter, the smaller is the range of breakdown voltages or times [89]. It is comparable to the inverse of the standard deviation, σ , of the Normal distribution, Cochran and Snedecor [89,127].

2.6.5 SEM and Image Tool Software for Surface Roughness Measurements

For SEM analysis, the magnet wires, having rectangular shape with smooth and rounded corners, are coated with different types of multi-layer insulation. For assessing the surface condition after aging, the SEM images are for a region of $\sim 13.3 \times 13.3 \mu\text{m}$.

The images are analyzed for the measurement of the erosion roughness by using an image tool software. To determine the surface roughness, after spatial calibration, the degraded areas are measured in nanometer scale. These measurements are then compared to the baseline values to report the relative surface roughness. The baseline values are determined before PD degradation of magnet wire enamel, which were selected randomly from their respective group.

In image tool software, measurements are displayed in a separate result window, with analysis features, like mean, and standard deviation. The software estimates the roughness by comparing the two surfaces before and after aging, as shown in Figure 2.18. The parameter used by the software is the dimensions of the detectable “dark areas”.

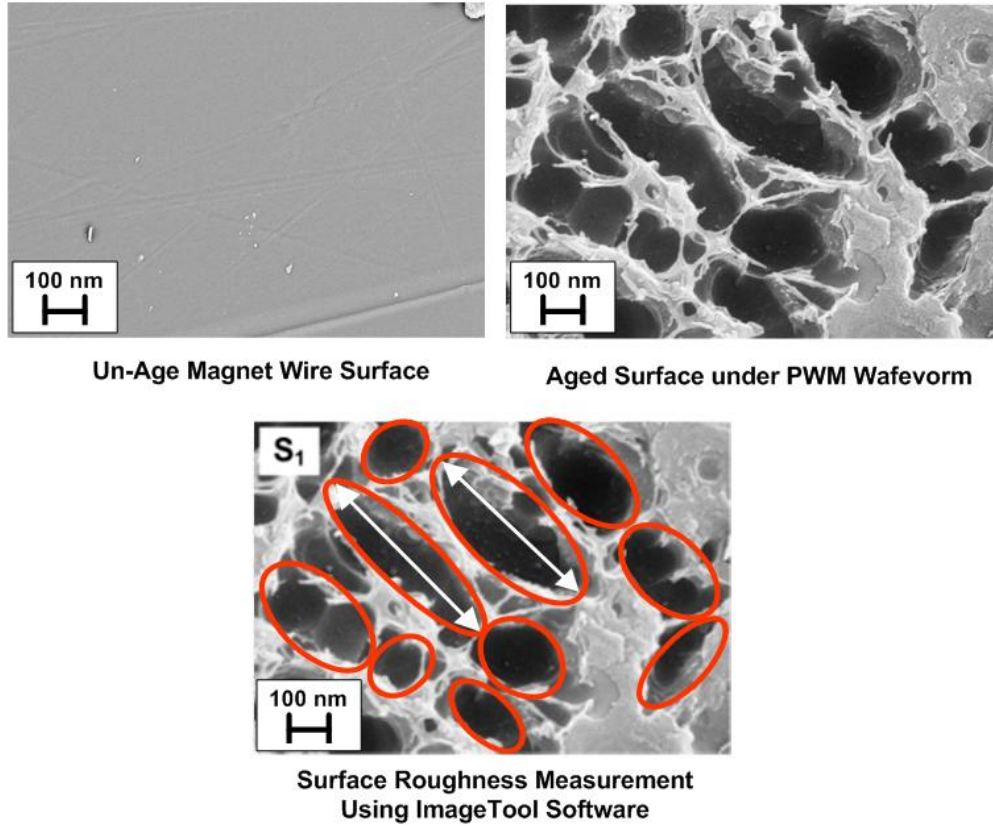


Figure 2.18 Comparison of SEM images for surface roughness measurements.

Chapter 3 Results

3.1 Introduction

In this chapter, using the test procedures described in Section 2.6, the test specimens prepared according to the procedures in Section 2.2 are evaluated for their performance under pulse applications. The aging results for the medium voltage induction motor inter-turn insulation, prepared with enamelled wires with polyimide and nanofilled coatings are done to understand the different mechanisms, in the insulation degradation. To assess the performance of the tested wire specimens, the residual strength is established by determining the dc breakdown voltages before and after aging. In addition, the TSDC results are given to provide information about the relaxation processes. TSDC results include the disorientation of the dipoles and the release of charges from the trapping sites in the enamelled wires. The principle objective is to establish a relationship between the space charge and the number of insulation layers of the magnet wire. Finally, the pulse aging results of the stator bar groundwall insulation with thermal analysis, and PD measurements are also presented.

3.2 Enamelled Wires Aging Test

Medium voltage induction motors are exposed to steep-front, non-sinusoidal voltages, when fed from PWM-VSC. Such steep-front voltage pulses propagate through the stator windings and impose stresses on the inter-turn insulation. This inter-turn stress is due to the fact that the distribution of the voltage across the motor coil is not uniform. The shorter the rise times of the pulse, the higher the frequency content and the greater the voltage across the turns of the winding. To understand the influence of such voltage stresses, the aging test results are discussed in two subsections: the results from testing the enamelled wire specimens subjected to steep-front pulse voltage waveforms and the results from testing under high frequency ac voltages. In each case, a group of 15

enamelled wire specimens from the same class are used [128]. To establish the residual strength of the wire specimens, dc breakdown voltages are recorded before and after the aging. As described in Section 2.3, the scatter of the breakdown voltage for both aged and un-aged samples, are analyzed by using a two-parameter Weibull distribution to determine the dc breakdown measurements.

3.2.1 Effect of Steep-Front Pulse Voltage Waveforms

In this section, the aging results of the conventional enamelled wire specimens, as well as the results of the laboratory developed wire specimens are described.

Conventional Enamelled Wires

The enamelled wires S_1 and S_2 are commercial materials. Enamelled wire, S_2 belongs to the family of corona resistant (CR) material, which has an additional coating of alumina filled THEIC (Tris-2-HydroxyEthyl IsoCyanurate) modified polyester resin. Before aging, the partial discharge inception voltage (PDIV) at 60 Hz ac of the enamelled wire specimens is determined by using the Haefely TE561 PD detector, (sensitivity level = 0.5 pC; bandwidth = 4-400 kHz). When the voltage is applied, a PDIV of approximately 900 V_p is usually observed for a 38 μm thick coating on a wire [63].

Each group of specimens is aged by unipolar steep-front pulses at different repetition rates (500 – 2000 Hz) for a voltage level of 1100 V_p for S_1 , and 750 V_p for S_2 , keeping the similar aging duration of 100 hours. It is commonly thought that during the manufacturing process of the wires, the coatings might have a number of defects that are distributed randomly [129]. These defects can additionally contribute to a weakness, which can result in lower values of the dielectric strength than those of theoretical values. Therefore, these premature failures are attributed to coating defects such as the improper thickness of the insulation, delamination, swelling, and cracks that occur during the manufacturing process. Figure 3.1 shows SEM images of some of the observed defects.

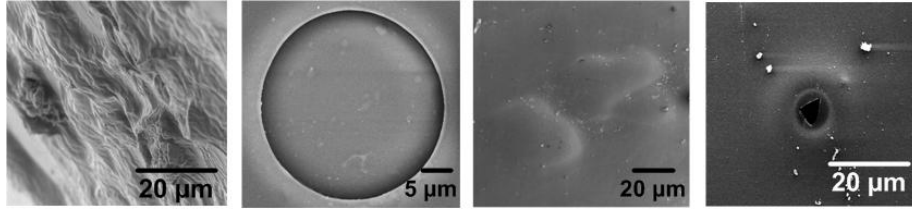


Figure 3.1: Defects found in magnet wire coatings.

As described in Sections 2.2.3 and 2.6.5, the dc breakdown voltages, η , along with the shape parameter, β , and standard deviation, σ , for S_1 and S_2 wires before and after the pulse voltage aging having duty cycle of up to 50%, are reported in Table 3.1.

Table 3.1: Parameters related to medium voltage conventional magnet wires S_1 and S_2 , subjected to different pulse switching frequencies.

Magnet Wire	Switching Frequency, f_s (Hz)	Scale Parameter, η (kV)	Shape Parameter, β	Standard Deviation, σ
S_1 (No Filler)	Un-Aged	11.12	7.16	1.41
	100	11.01	7.20	1.53
	200	10.99	6.11	1.67
	400	10.95	5.10	1.92
	500	9.91	4.95	2.46
	1000	9.90	3.41	2.94
	1500	9.40	3.03	3.19
	2000	8.90	2.73	3.31
S_2 (Alumina)	Un-Aged	7.61	5.47	1.90
	100	7.40	3.17	1.89
	200	7.39	3.12	2.01
	400	7.38	3.11	2.05
	500	7.35	3.08	2.13
	1000	6.10	3.09	2.15
	1500	5.30	3.10	2.29
	2000	4.65	3.02	2.43

The Weibull plot for enamelled wire S_1 depicted in Figure 3.2, shows variation of dc breakdown voltage for un-aged, and at pulse switching frequencies of 1000 and 2000 Hz. According to the Weibull distribution, the value of the dc breakdown voltage corresponds to a 63.2% breakdown cumulative probability. To attain the best fit of the experimental data, the maximum likelihood estimation with a 90% confidence bound interval is used, as a 10% risk is reasonable from a statistical point of view [91,93]. In all cases, the fit of the experimental data, r^2 , is observed to be in the range of 0.9 to 0.95. The dc breakdown voltage experiment proves that there is no significant difference between the positive and negative polarity voltages indicating that the field is nearly uniform between the two turns [126]. Therefore, for all the breakdown tests and to evaluate the insulation performance, a positive polarity is adopted.

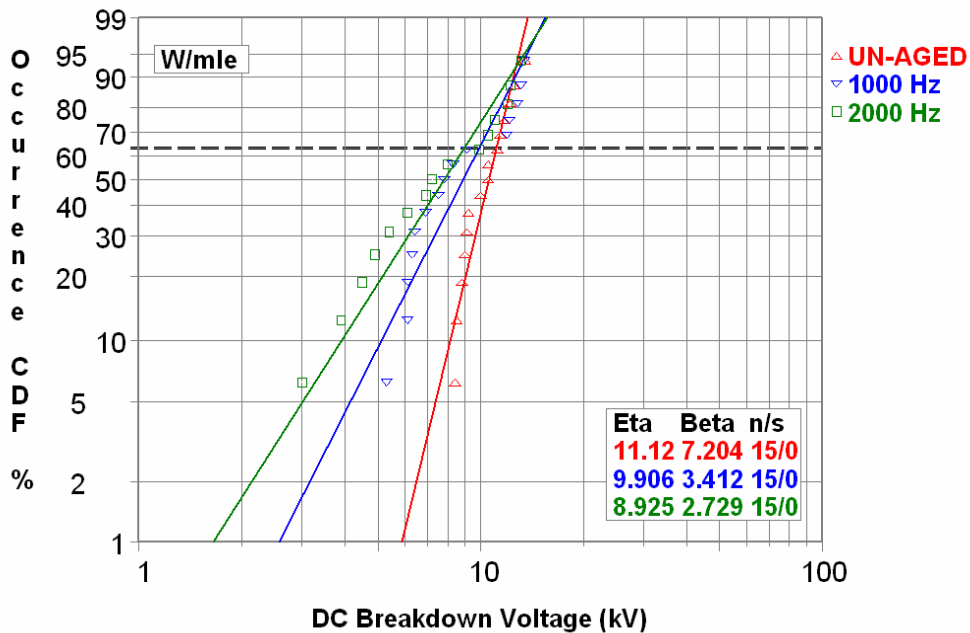


Figure 3.2: Weibull probability distribution plot of the dc breakdown voltages for wire S_1 at different pulse switching frequencies.

The test results listed in Table 3.1 are further depicted in Figure 3.3 to see the variation in breakdown strength as a function of frequency. The results reveal that more than one degradation process needs to be considered for both the S_1 and S_2 samples, as

suggested by the two distinct slopes. The two principal regions, based on the pulse repetition rate, correspond to the change in the aging mechanisms [13]. It is believed that the contribution of the charge accumulation, in addition to the PD activity, can result in two distinct slopes, as depicted in Figure 3.3.

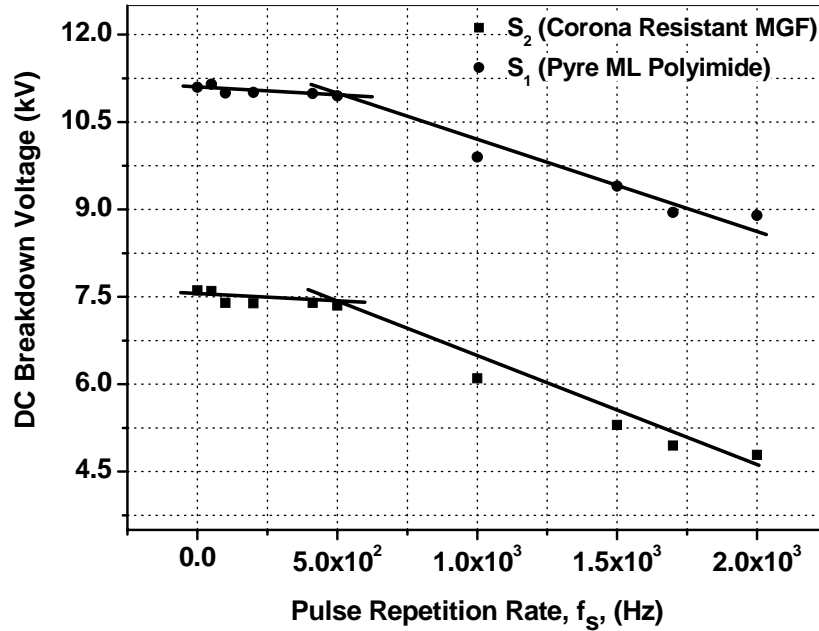


Figure 3.3: Residual life based on the dc breakdown voltage for conventional wires aged by unipolar steep-front pulses at different repetition rates (aging voltage $S_1 = 1100 V_p$; $S_2 = 750 V_p$ for ~ 100 h duration).

The data listed in Table 3.1 for Weibull shape parameter β and standard deviation σ , for magnet wire S_1 , is also included in Figure 3.4. The standard deviation depends on the number of samples in the test and appears to be most disturbing for β . The results demonstrate that an inverse relation, between the two parameters, exists. In Figure 3.4, the distance between these two parameters decreases as the pulse repetition rate increases. The higher scatter of data is observed at higher switching frequencies due to the increase of the randomly distributed defects. The inserted log-log plot in Figure 3.4 reflects a relation between relative standard deviation σ/β and the pulse repetition rate. The data

fits quite well and exhibit an almost exponential increase. It is evident that the higher pulse switching frequency leads to increased scatter, and thus, a higher deviation in the data. The domination of the standard deviation over the shape parameter is due to the response of the multi-layer coatings on the magnet wire. This can be attributed to the different aging mechanisms, which are causing the accelerated degradation. Almost, similar results are observed for magnet wire S_2 .

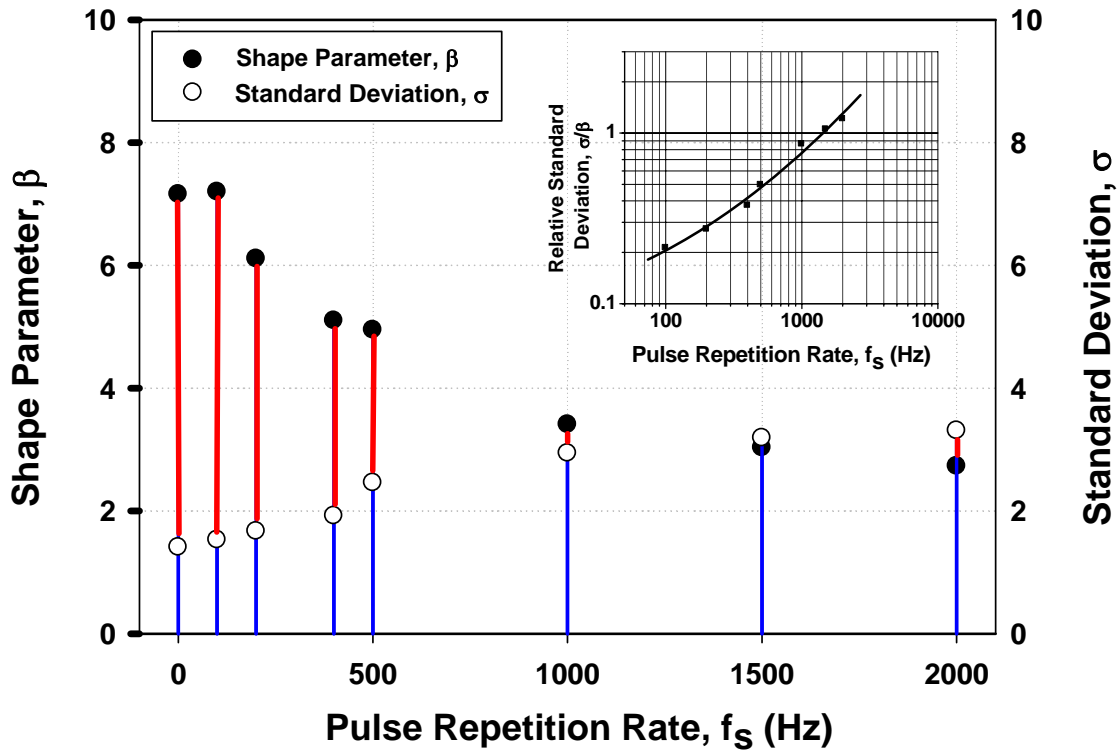


Figure 3.4: Variation in the shape parameter β and standard deviation σ for magnet wire S_1 under different pulse repetition rates. The log-log sub-plot shows the relation between the relative standard deviation σ/β and pulse repetition rate.

Laboratory Developed Enamelled Wires

The experimental results, as shown in Figures 3.3 and 3.4, suggest that the degradation process is due to both the PD and charge accumulation/trapping; thus, the analysis of the new enamelled wires, listed in Table 3.2, should be considered in detail [130]. The effect of the pulse aging on the newly prepared wires, which belong to the same class as of S_1 ,

is evaluated by measuring the dc breakdown voltages. The results, presented in Figure 3.5, indicate that in the new wires; S_{1A} , S_{1B} , S_{1C} , and S_{1D} , the residual life decreases with the increase of the insulation layers on the magnet wires. In addition, for the S_{1D} wire, two main regions, based on the pulse repetition rate, are observed. This corresponds to the change in the aging mechanisms, as shown in Section 3.2.1 for wires S_1 and S_2 . The contribution, by the slow degradation process that is charge trapping and the accumulation in the bulk of multi-layer insulation systems of enamelled wires is presented in Section 3.4 by using the technique of TSDC.

Table 3.2: Dimensional and electrical parameters, related to magnet wires having coating type polyimide, Pyre-ML®, before aging (Reference Data).

Type	Number of Insulation Layers	Insulation Thickness [μm]	DC Breakdown Voltage [kV]
S_{1A}	1	7.2	0.615
S_{1B}	2	13.0	1.169
S_{1C}	3	19.0	1.620
S_{1D}	4	24.2	1.912

3.2.2 Effect of High Frequency AC Waveforms

For high frequency ac tests, the dc breakdown voltages of both conventional (S_1 and S_2) and the custom designed enamelled wires (S_{1A} , S_{1B} , S_{1C} , and S_{1D}) are determined, after aging, by the various sinusoidal frequencies of 60 Hz, and 2-4 kHz for ~100 h. It is obvious from Figures 3.6 and 3.7 that the selected test frequency range plays a different role on the aging process. Further, the drop in the dc breakdown voltage is high for the magnet wires with the higher number of insulation layers, compared with the samples aged under pulse voltages. The dc breakdown voltage decreases almost linearly, as the frequency of test voltage is increased from 60 Hz to 4 kHz. This decrease is attributed to the degradation due to the enhanced PD activity between the gaps of the enamelled wires, and the heat build-up due to the dielectric loss.

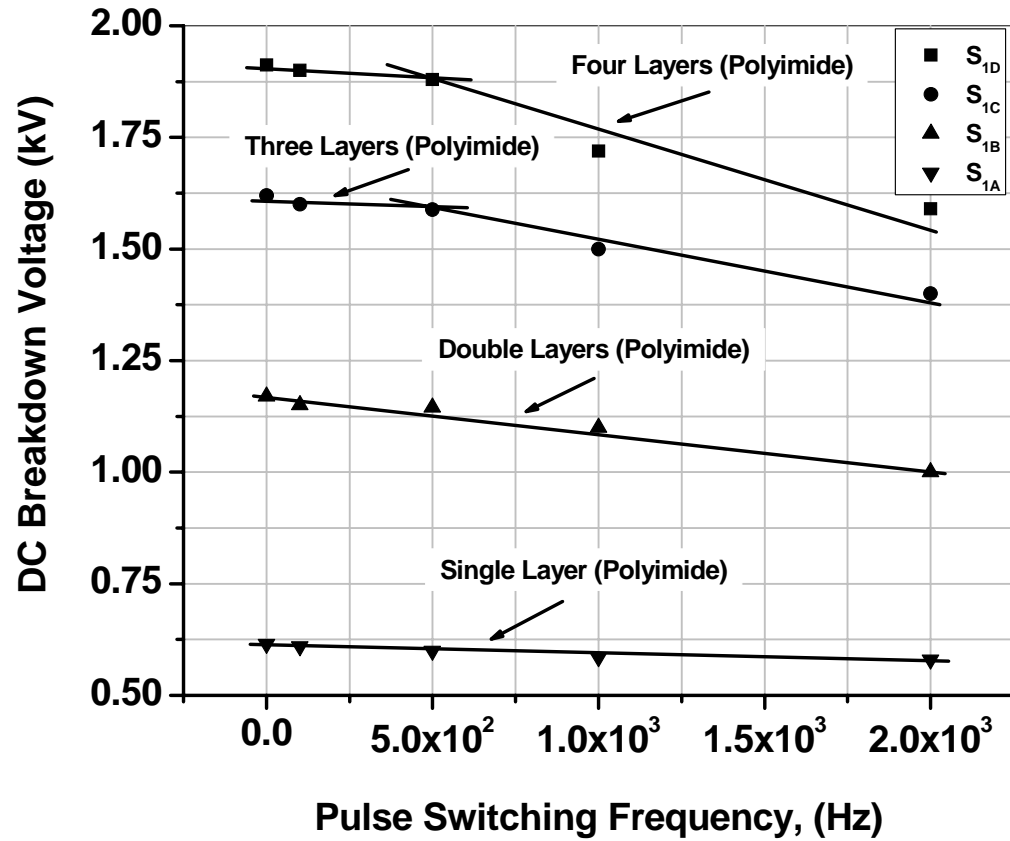


Figure 3.5: Residual life based on the dc breakdown voltage for laboratory developed wires, aged by unipolar steep-front pulses at different repetition rates (test voltages, $S_{1A} = 215 V_p$; $S_{1B} = 390 V_p$; $S_{1C} = 570 V_p$; $S_{1D} = 720 V_p$ for ~ 100 h duration).

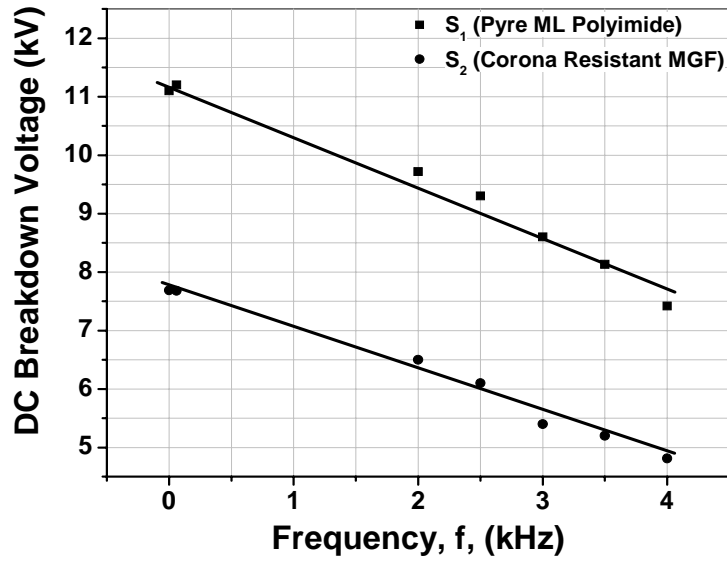


Figure 3.6: Residual life based on the dc breakdown voltage for conventional wires (S_1 and S_2) aged under high frequency ac waveforms at a constant electric stress of 30 kV/mm peak for ~ 100 h duration.

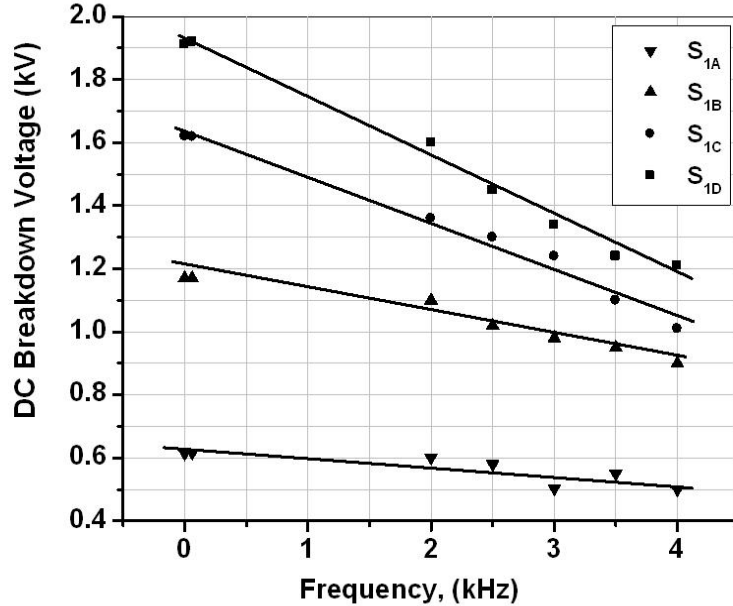


Figure 3.7: Residual life based on the dc breakdown voltage for laboratory developed wires aged under high frequency ac waveforms at a constant electric stress of 30 kV/mm peak for ~ 100 h duration.

3.3 Magnet Wires PD Erosion Tests

In this section, the results, relevant to the effectiveness of nanofillers on the erosion resistance of enamelled wires, are considered. The procedure, described in Section 2.6.5, is applied to the magnet wire specimens, as described in Section 2.2. The results in terms of the surface roughness for the aged samples are measured. For the PD erosion that results from the medium voltage (2.3-6.6 kV) PWM drives, a real PWM-VSC, 10 kV peak-to-peak, low power single-phase generator [131] is used to test the samples. Figure 3.8 signifies a PWM waveform, generated by the custom-built supply, with a fundamental frequency of 60 Hz and a switching frequency of 1.25 kHz.

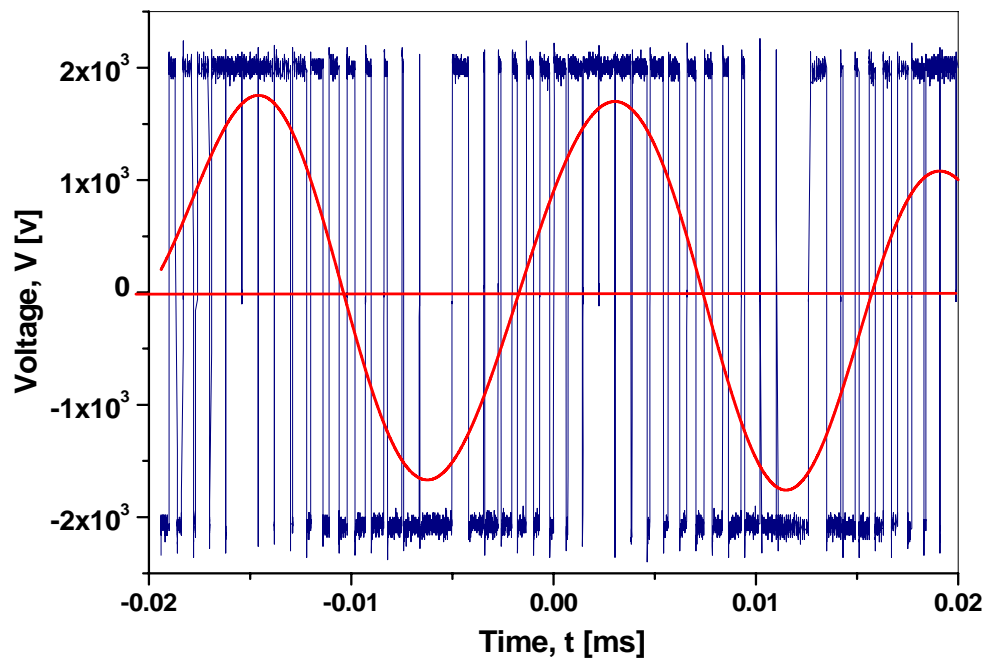


Figure 3.8: PWM waveform from a PWM generator used for testing of magnet wire specimens (S_1 to S_6).

3.3.1 PWM-VSC Aging

The magnet wire specimens (S_1 to S_6), examined for PD resistance, are exposed to a stress of 100 kV_p/mm for 1 h under PWM-VSC waveforms. Table 3.3 lists the average,

CHAPTER 3. RESULTS

mean, and standard deviation of the results. From the results in Figure 3.9, the higher relative surface roughness of approximately 1195 with a standard deviation of 134.5 is observed for enamelled wire S_1 without nanofillers. Similarly, wires S_2 and S_3 , which are commercially available PD resistant wires, reveal similar surface erosion, after comparing both un-aged and aged samples. The relative surface roughness is around 327 for S_2 and 313 for S_3 , along with the piling up of nanoparticles, to reduce the PD attack [132]. Also, the standard deviation values are lower, compared with wire S_1 , which are 63 and 45.5, respectively.

In magnet wires S_4 , S_5 , and S_6 , filled with fumed silica (SiO_2), TiO_2 , and Al_2O_3 , respectively, the relative surface erosion, due to the PD, is comparatively lower. In magnet wires S_4 and S_5 , the relative PD erosion seems to be around 240 and 280, respectively. In addition, in both cases, the scatter in the data is smaller; whereas, in comparison, S_6 shows surface erosion relatively higher in the range of 322 with a standard deviation of 52.5.

Table 3.3: Average, mean, and standard deviation of the relative surface roughness in magnet wire coatings subjected to PWM-VSC waveforms at 100 kV_p/mm.

Magnet Wire	Nanofillers	Relative Surface Roughness		
		Average	Mean	Standard Deviation, σ
S_1	-	1195	1166	134.5
S_2	Alumina	327	322	63.0
S_3	Alumina	313	320	45.5
S_4	Fumed silica	240	230	35.5
S_5	Titanium oxide	280	270	38.8
S_6	Alumina	322	313	52.5

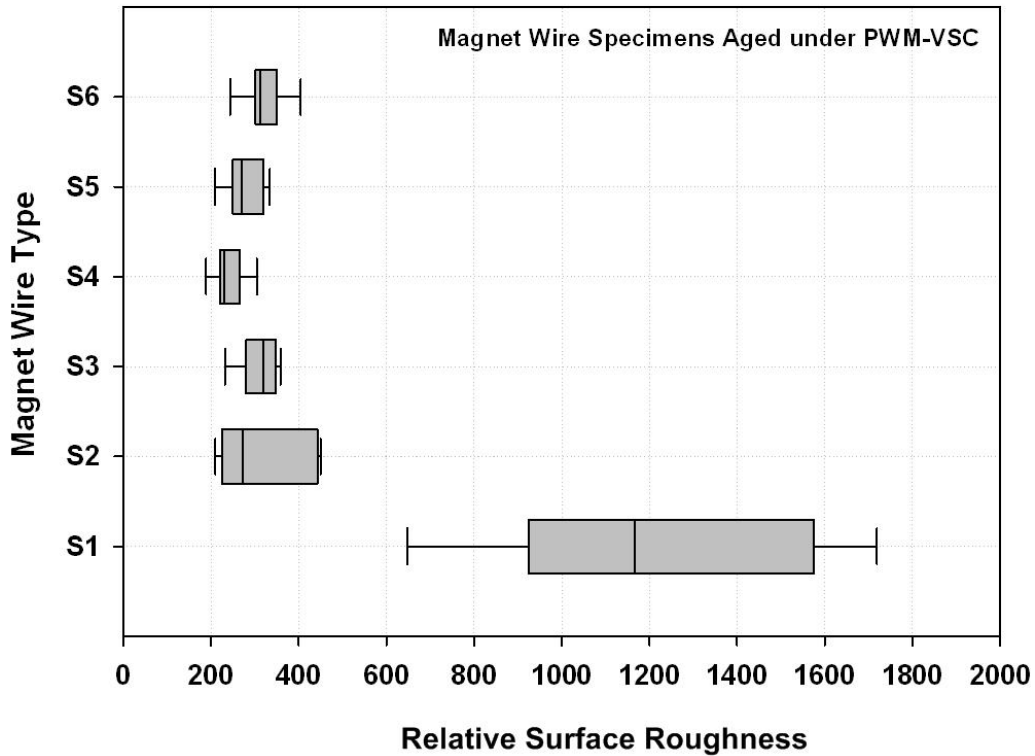


Figure 3.9: Summary of the PD erosion test results for magnet wires (S_1 to S_6) aged under PWM-VSC waveform at a constant stress of $100 \text{ kV}_p/\text{mm}$ ($f_s = 1.25 \text{ kHz}$). Bar mark the 5 and 95 percentiles; the extremities of the hatched box are 25 and 75 percentiles and the centre line represents the average of the data.

3.3.2 High Frequency AC Aging

The properties of magnet wires S_1 to S_6 are also examined at 10 kHz ac with a constant stress of $70 \text{ kV}_p/\text{mm}$ for a one-hour duration. Table 3.4 lists the average, mean, and standard deviation of the results. From the results that are represented in Figure 3.10, severe surface erosion is observed in all of the commercial magnet wires, S_1 , S_2 , and S_3 , after aging. A comparative investigation indicates an average relative roughness of approximately 701 in wire S_1 ; wires S_2 and S_3 , commercially available PD resistant wires, portray relative surface erosion as high as 176 and 127, respectively. The surface

erosion in S_3 is comparatively lower in the case of high frequency ac waveforms because of the new polyimide film, which is specifically designed to withstand the damaging effect of PD activity [83]. In magnet wires S_4 and S_5 , filled with fumed silica (SiO_2) and TiO_2 , the surface erosion due to PD, is almost negligible under high frequency ac waveforms. In both cases, the relative surface erosion is observed to be in the close range of 12. For wire S_6 , with Al_2O_3 nanofillers, the relative surface erosion is comparatively higher and observed to be approximately 37.

Table 3.4: Average, mean, and standard deviation of the relative surface roughness in magnet wire coatings subjected to high frequency ac waveform at 70 kV_p/mm .

Magnet Wire	Nanofillers	Relative Surface Roughness		
		Average	Mean	Standard Deviation, σ
S_1	-	701	720	88.8
S_2	Alumina	176	187	56.2
S_3	Alumina	127	119	41.2
S_4	Fumed silica	12	13	4.5
S_5	Titanium oxide	12	12	5.2
S_6	Alumina	37	36	8.1

The experimental results demonstrate that nanofillers are more resistant to PD, when they are used in the polymers. Also, the results confirm that the addition of a small amount of nanofillers is sufficient to improve the PD resistance. The comparative results indicate that under PWM-VSC aging conditions, the surface degradation in magnet wire coatings is much greater. This can be attributed to the stresses, due to the high dV/dt of the PWM waveforms. In the case of the high frequency ac aging, standard deviation σ of surface roughness is measured for wires S_1 to S_6 . The higher value of 88.8 is measured for wires without nanofillers. For wire specimens with nanofillers, the standard deviation is very small; the scatter in the data, recorded for S_4 , is only 4.5.

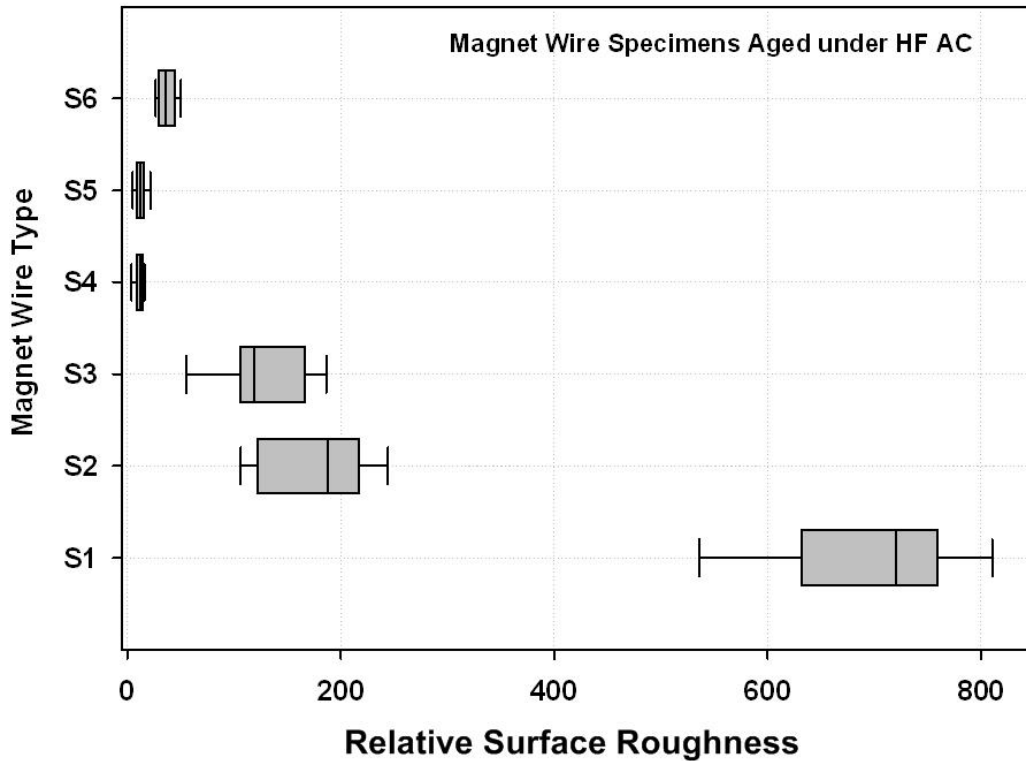


Figure 3.10: Summary of the PD erosion test results for magnet wires (S_1 to S_6) aged under high frequency ac waveform at a constant stress of $70 \text{ kV}_p/\text{mm}$ ($f = 10 \text{ kHz}$). Bar mark the 5 and 95 percentiles; the extremities of the hatched box are 25 and 75 percentiles and the centre line represents the average of the data.

3.3.3 Residual Insulation Strength

The specimens described in Section 2.2, are also tested for a comparative evaluation of the wire's residual life under a high frequency ac. The residual life is established by measuring the dc breakdown strength before and after aging, by following the procedure described in Section 2.3. Figure 3.11 displays a comparison of the changes in the dc breakdown strength for the wires with and without nanofillers. Since all the tests involve different test voltage amplitudes, a constant electric stress must be maintained across the insulation for the different wires and different frequencies.

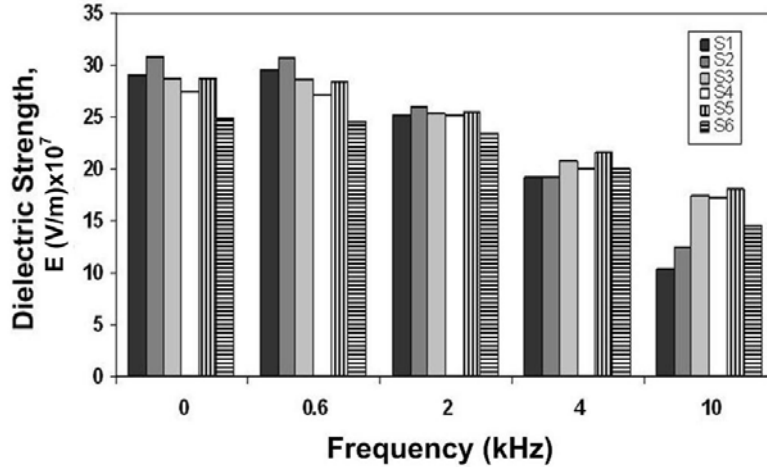


Figure 3.11: Variations in the dielectric strength of magnet wires (S_1 to S_6) by increasing the ac frequency.

The dispersion of the dielectric strength data is found to be smaller, and the values are closely clustered in a frequency range up to 4 kHz with a standard deviation of 2.24. However, at a higher frequency, 10 kHz, the dispersion in the data is larger for commercial wires S_1 , S_2 , and S_3 with the standard deviation values in the range of 6.9 to 7.5. For the laboratory-developed wires, due to the small scatter in the data, the standard deviation at 10 kHz is lower, in the range of 3.2 to 4.9. Although the results are difficult to compare, such high frequency tests lead to quick results that indicate the quality and characteristics of the coating material. For the PD resistant wires, the maximum variations in the dielectric strength are in magnet wire S_2 , 65%; whereas, S_4 and S_5 exhibit a similar change in the breakdown voltage, 37%. For the commercially filled wires, S_3 exhibits the best resistance to PD, and its breakdown voltage changes as much as 40%.

3.4 Thermally Stimulated Depolarizing Currents (TSDC) in Magnet Wires

The procedure, described in Section 2.6.3, is applied to magnet wire specimens S_1 with Polyimide (Pyre-ML® RC-5019) coatings. Before the specimens are used, they are heat-

treated for 3 hrs at 200 °C to remove any moisture and to improve the reproducibility of the results. TSDC measurements are carried out to study the mechanisms, charge storage and the subsequent release from the bulk of the magnet wire coatings. The currents reveal a number of peaks, reflecting the processes which are related to molecular relaxation and the delocalization of the charges injected into the polymer bulk during polling [133].

Table 3.5 lists different conditions for which the TSDC spectra are obtained for magnet wire specimens S_1 . Later, these spectra are utilized for the estimation of the parameters such as activation energy ε_a characteristic relaxation time τ , and charge released Q , during the relaxation process.

Table 3.5: Test conditions for TSDC measurements.

Type of Investigation	Thickness [μm]	T_P ($^{\circ}\text{C}$)	Charging Time t_p (min)
Long-Term Aging Effect @ 1 kV peak, for 6 to 100 h	38.4	155	360-6000
Effect of Unipolar Polling Voltage from 1.0 to 3.5 kV peak	38.4	120	60
Effect of PWM-VSC @ Polling Voltage 1.0 to 2.25 kV peak	38.4	120	60
Effect of Multiple Layers @ $E = 5$ kV/mm peak (1-9 Layer)	7.2–54.1	100	60

3.4.1 Long-Term Aging Effect (t_p)

The TSDC curves, for the commercially available type ML enamelled wire S_1 , are shown in Figure 3.12. As seen, increasing the polling time (t_p) from 6 to 100 h results in higher peaks. The eight-hour unipolar pulse-aging curve offers two peaks: one at 70 °C and the other at 95 °C. Similar behaviour is observed for the specimens, aged by longer durations. As the polling time increases, more charges are accumulated in the distributed traps, causing an increase in the amplitude of these peaks.

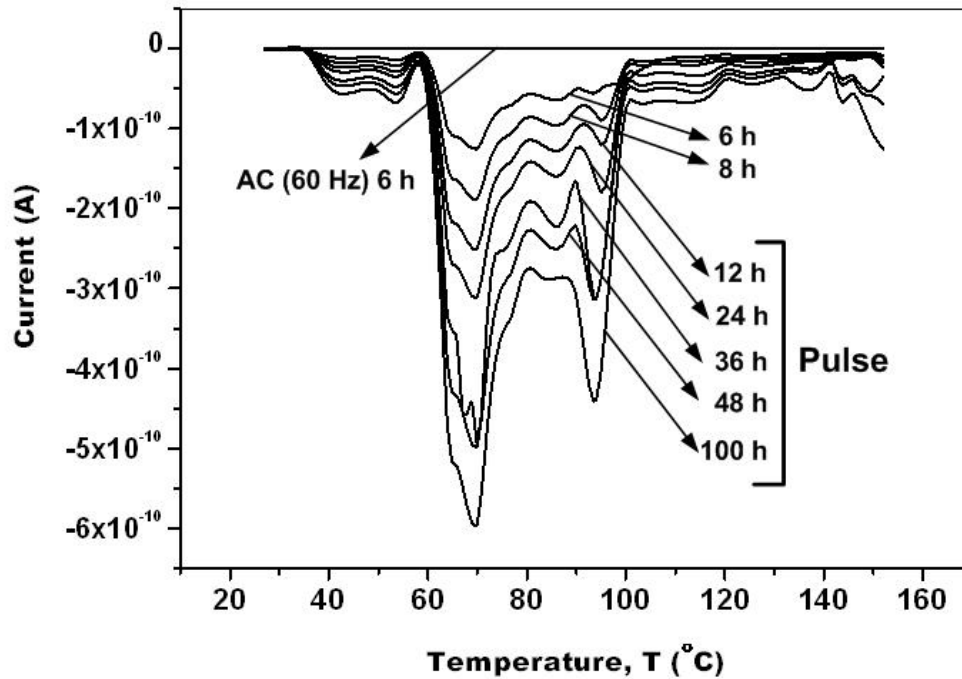


Figure 3.12: TSDC results for time dependence pulses aged at 1 kV peak (pulse repetition rate – 2 kHz).

Furthermore, by increasing the polling time to 100 h, the low temperature current peak at 70 °C becomes more pronounced than that at a higher temperature. Figure 3.12 also confirms that the origin of this peak is obviously related to free or shallow trapped charges, which are injected from the electrodes and accumulate in the boundaries of the magnet wire coating. Neagu *et al.* [134] and Sussi *et al.* [116] report similar behaviour for TEFZEL® and in KAPTON®, suggesting that the shallow trap density is probably greater than that of deeper traps [135].

Also, the elevated temperature and fast repetitive voltage pulses can lead to microscopic structural modification of the wire insulation. Such detectable changes and structural modification of the wire insulation may lead to trap formation that increases slowly with the length of the aging time. In Figure 3.13, the released charge (the area under the peaks) from the trap sites increases linearly with the increased aging time and slows down after 48 hrs. This is attributed to the permanent structural modification of the

wire insulation, which creates predetermined localized trap sites. It is believed that further aging might cause an increase in the concentration of the accumulated charges; however, similar behaviour as shown in Figure 3.15, is also reported by Fu *et al.* [136] for low-density polyethylene (LDPE) under ac aging.

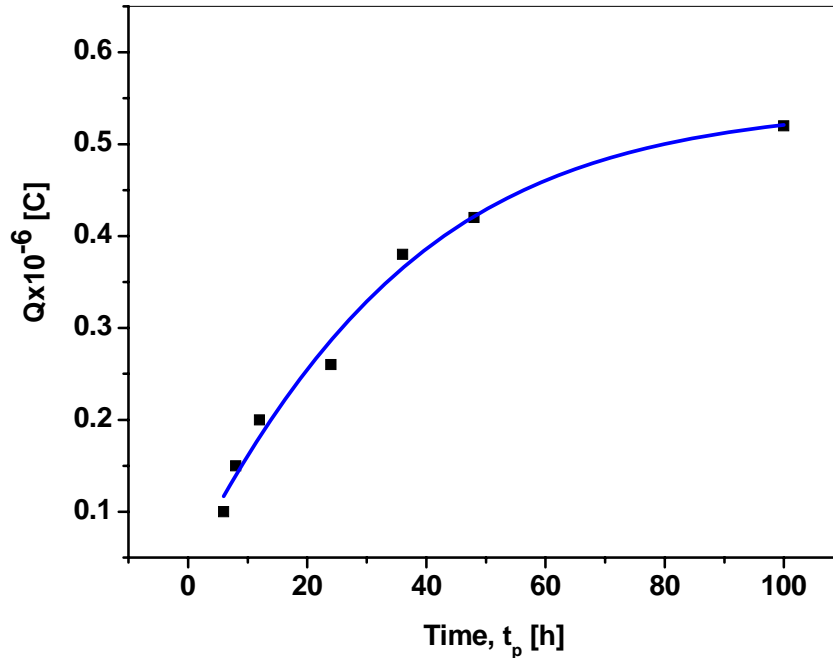


Figure 3.13: Total charge vs. polling time for magnet wire S_1 .

3.4.2 Influence of Polling Field (E_p)

Figure 3.14 illustrates the TSDC curves for the multi-layered commercial magnet wire S_1 with a polyimide type ML coating with a thickness of $38.4 \mu\text{m}$. The specimens are polarized at 120°C for the different steep-front pulse voltages ranging from 1 to 3.5 kV peak with a duty cycle as high as 0.5 and by a pulse repetition rate of 2 kHz. The TSDC measurements are obtained with a heating rate of $2\text{-}3^\circ\text{C}\cdot\text{min}^{-1}$. All the TSDC peaks occur in the temperature range of 70 to 170°C . In Figure 3.14, curves 1 and 2 represent the current release from a specimen, polarized for one hour at 1 kV and 1.5 kV peak, respectively. In both cases, the observed peaks are relatively small. However, the specimens polled at 120°C and 2.5 to 3.5 kV peak reflects four distinct peaks (curves 3-

